

Supplementary Materials for

A hybrid plasma electrocatalytic process for sustainable ammonia production

Jing Sun¹, David Alam², Rahman Daiyan¹, Hassan Masood¹, Tianqi Zhang², Renwu Zhou²,
Patrick J. Cullen², Emma C. Lovell^{1*}, Ali (Rouhollah) Jalili^{1*} and Rose Amal^{1*}

¹School of Chemical Engineering, University of New South Wales (UNSW), Sydney, Australia.

²School of Chemical and Biomolecular Engineering, University of Sydney, Sydney, Australia

Correspondence to: e.lovell@unsw.edu.au, ali.jalili@unsw.edu.au, r.amal@unsw.edu.au

This PDF file includes:

Materials and Methods
Supplementary Text
Figs. S1 to S22
Tables S1 to S4
Captions for Movies S1 to S6

Other Supplementary Materials for this manuscript include the following:

Movies S1 to S6

Materials and Methods

Materials

All reagents and solvents were purchased from Sigma-Aldrich or from Chem-Supply Pty Ltd. Cu foam was purchased from Xiamen TMAX Machine Limited. Oakton pH/Ion 700 Ion 700 Benchtop Meter and Cole-Parmer Combination Ion Selective Electrodes (nitrate) were purchased from John Morris Group. Milli-Q water with a resistivity of 18.2 M Ω .cm was obtained from an inline Millipore RiOs/Origin H₂O purification system, was used throughout the experiments for sample preparation and reaction. ¹⁵N₂ was purchased from Sigma-Aldrich (SKU No: 364584-5L).

Methods

Copper nanowires (Cu NWs) fabrication. The commercial Cu foam and foil was cut into desired sizes and ultrasonically cleaned with acetone, ethanol, and finally Milli-Q water for 15 min intervals, and then washed with dilute H₂SO₄ solution to remove any surface impurities and oxide layers. Cu(OH)₂ nanowires were first synthesized on Cu foam by immersion into a solution containing 0.133M (NH₄)₂S₂O₈ (ammonium persulfate) and 2.667m NaOH for 0.5 h at room temperature. Subsequently, the Cu foam was removed out from solution, rinsed with Milli-Q water and absolute ethanol, and air-dried. CuO NWs were then fabricated by annealing the prepared Cu(OH)₂ NW arrays at 180°C for 1 h in air. The resulting CuO NWs sample was electrochemically reduced to Cu/Cu₂O NW arrays in 0.5M Na₂SO₄ under -1V vs RHE.

Physical characterization. X-ray photoelectron spectroscopy (XPS) was performed on a Thermo Scientific K-Alpha X-ray spectrometer. The morphology and structure of Cu NWs were imaged by scanning electron microscopy (SEM) using a JEOL JSM-IT-500 HR. UV-Vis. Absorption spectrum were recorded on a Shimadzu UV-3600 UV-VIS-NIR spectrophotometer.

Electrochemical evaluation. All electrochemical evaluations were conducted using Autolab Potentiostat (Autolab M204) in a custom-designed H-type electrochemical cell and electrolyzer. The cathodic chamber was separated from the anodic chamber by Nafion@117 membrane (purchased from fuel cell store). For the H-type cell, a three-electrode set-up with the Cu catalyst (foil, foam, and Cu NWs) as the working electrode (WE), platinum wire as the counter electrode (CE) and Ag/AgCl (*sat.* KCl) as the reference electrode (RE) was used. 10 mM H₂SO₄ was used as the background electrolyte in this study, and the optimization of acid concentration was performed. Typically, for the H-type cell studies, 50 mL of electrolyte was used in the cathodic chamber to allow for electrolyte sampling. The electrode size for the H-cell was 1cm² and Cu foil was used for optimization studies. The reaction was facilitated with magnetic stirrer at the speed of 650 rpm. All potentials for H-type cell were described versus the reversible hydrogen electrode (RHE) via the following equation:

$$E_{RHE} = E_{(Ag/AgCl)} + 0.197 + 0.059 \times pH \quad (pH = 1.68 \text{ in this study})$$

To further translate this concept for large scale application, we fed the plasma-activated water (PAW) from the scaled-up reactor (*vide infra*) into a high throughput electrolyzer to understand the potential for ammonia production rate and yield. Herein, we prepared a membrane electrode assembly (MEA) by sandwiching the Cu NWs cathode (electrode size 9 cm²) and DSA[®] anode (purchased from Industrie De Nora S.p.A.) between a commercial Nafion membrane. The MEA was loaded within the electrolyzer with PAW being used as the

catholyte and 0.1 M H₂SO₄ as the anolyte (using a peristaltic pump with a flow rate of 1.5 mL/min). For the electrolyzer optimization, 250 mL of the PAW was circulated in the cathodic chamber. For the stability test, a continuous flow was used for 8 h with 30 mA/cm² being applied.

Ammonia (as ammonium NH₄⁺) detection by the indophenol blue method. From the cathodic chamber electrolyte solution, 0.5 mL of electrolyte was taken and transferred into a 2 mL sample tube. Into the tube, 0.4 mL of 1 M NaOH solution (with 5 wt.% salicylic acid and 5 wt.% sodium citrate), 0.1 mL of 0.05 M NaClO and 30 μL of 1 wt.% C₅FeN₆Na₂O (sodium nitroferricyanide) in water was added. The mixture was then incubated in the dark at room temperature for 2 h prior to UV-Vis testing. The concentration of ammonia was determined via a calibration curve. The calibration curve was prepared using a set of standard solutions with a known amount of (NH₄)₂SO₄ (concentrations were based on NH₄⁺) in 10 mM H₂SO₄. Into these solutions, the above-mentioned indophenol blue reagents were added, and the indophenol blue absorbance at 655 nm was determined after 2 h. The limit of detection (LOD) of UV-Vis used in this study refers to the absorbance at 655 nm obtained from blank 10 mM H₂SO₄ for the lower limit and from 200 μM NH₄⁺ for the upper limit.

Nitrite (NO₂⁻) detection by Griess Reagent. 50 μL of the sample was taken and transferred into a cuvette and combined with 50 μL of Griess Reagent and 0.9 mL of Milli-Q water. The resulting sample was mixed thoroughly. The mixture was incubated at room temperature in the dark for 0.5 h prior to UV-Vis testing. Solutions of NaNO₂ with known concentrations (in 10 mM H₂SO₄) were used as calibration standards, with the absorbance at 525 nm used to plot the calibration curves. Upper LOD of UV-Vis used in this study refers to the absorbance at 525 nm obtained from 200 μM NaNO₂. A dilution factor was applied to measure nitrite concentration in plasma-activated water (PAW).

Nitrate (NO₃⁻) detection by ion-selective electrode. An ion-selective electrode (ISE), also known as a specific ion electrode (SIE), is a transducer (or sensor) that converts the activity of a specific ion dissolved in a solution into an electrical potential. The voltage is theoretically dependent on the logarithm of the ionic activity, according to the Nernst equation. Cole Palmer Nitrate selective probe has a concentration range of 7 μM to 1 M (0.5 to 62,000 ppm). The ionic strength of ion solutions varies with the concentration of the ion to be measured. To maintain a constant ionic strength, an Ionic Strength Adjuster (ISA) is added. This ensures the total ionic strength is independent of the analyte concentration. In this study, 2 M ammonium sulphate (NH₄)₂SO₄ was added, as the ISA, at 400 μL to each 20 mL of standard or sample to adjust the ionic strength to about 0.12 M.

H₂ detection by gas chromatograph (GC). H₂ detection was tested by GC (Shimadzu, Model 2010 Plus) equipped with both a thermal conductivity detector (TCD) and flame ionization detector (FID).

Nuclear magnetic resonance (NMR). To detect the liquid products, 0.65 mL of aliquot was collected at the end of each bulk electrolysis at fixed potentials and was analyzed using a 600 MHz ¹H liquid NMR spectrometer (Bruker Avance) at 25 °C. The ¹H spectrum was measured with water suppression method.

¹⁵N₂ isotope labeling experiment. To demonstrate that the resultant ammonia/ammonium originates from the source of N₂ gas rather than potential contamination, ¹⁵N₂

isotopic experiments were carried out, with the ammonia/ammonium detected by ^1H NMR to distinguish between $^{15}\text{NH}_4^+$ and $^{14}\text{NH}_4^+$.

Control Ar and $^{14}\text{N}_2$ experiments as well as $^{15}\text{N}_2$ isotopic experiments were carried out in a sealed H-cell set-up with the two chambers being separated using a Nafion membrane. Each chamber contained 50mL of 10mM H_2SO_4 . The cathodic chamber was first purged with O_2 gas for 15 mins then filled with 50 mL oxygen (Coregas, >99.9 %). A balloon containing ~200 ml of the feed gas being $^{15}\text{N}_2$ (Sigma-Aldrich, 98 atom%) or $^{14}\text{N}_2$ (Coregas, >99.995%) or Ar Coregas, >99.997%) was connected to the cell to be mixed with the O_2 in the chamber. The $^{15}\text{N}_2$ gas was purified by passing through an acid trap (10mM sulfuric acid) to remove any possible contaminants, including $^{15}\text{NO}_x$ and $^{15}\text{NH}_3$, before being collected.

A pin electrode for plasma was used to simulate the bubbler. The plasma was generated for 0.5 h, at a voltage of 120V, duty of 83 μs , discharge frequency of 600Hz and resonance frequency of 60Hz. For the subsequent electrocatalysis, a three-electrode set-up was used with the Cu NWs as the working electrode (WE), a Pt wire as the counter electrode (CE) and Ag/AgCl (sat. KCl) as the reference electrode (RE). The electrocatalysis was run at -0.5V vs RHE for 0.5 h, with samples taken at fixed intervals.

Samples were analyzed using a 600 MHz ^1H liquid NMR spectrometer (Bruker Avance) at 25 °C. The ^1H spectrum was measured with a solvent (water) suppression method and 128 scans (16mins49s).

Faradaic efficiency and production rate calculations. The two crucial descriptors, revealing ammonia synthesis performance, are the Faradaic efficiency and the ammonia production rate. The *Faradaic efficiency* indicates the selectivity of the electrocatalysis for ammonia synthesis, which refers to the ratio of the electrical energy consumed for the synthesis of ammonia to the overall energy through the electrochemical system. The Faradaic efficiency (η) of ammonia synthesis was determined by Eq. (S1), where n is the figure of the desired electrons for synthesizing one ammonia molecule ($n = 6$ when ammonia is from nitrite and $n = 8$ when ammonia is from nitrate), F is the Faraday constant ($F = 96485.33$), C is the detected ammonia molar concentration, V is the electrolyte volume, and Q is the overall electrical energy travelled over the electrodes. To calculate the number of the exchanged electron, both nitrite and nitrate concentrations were measured before and after each reaction; the average found to be 7.6. For the reactions that both nitrite and nitrate are fully exhausted, n was calculated based on their initial ratio.

$$\eta = \frac{n \cdot F \cdot C \cdot V}{Q} \quad (\text{Eq. S1})$$

Ammonia production rate (R) is the ammonia production over unit time and over unit electrode surface area. It can be determined by Eq. (S2), where C is the detected ammonia molar concentration, V is the electrolyte volume, t is the reaction time, and S is the catalytically active surface area of the electrode.

$$R = \frac{C \cdot V}{t \cdot S} \quad (\text{Eq. S2})$$

The electric power required to convert NO_x intermediary to ammonia is calculated by Eq. (S3), where P is power in watts (W), V is voltage in volts (V) and I is current in amps (A). In the electrolyser, a certain voltage (difference between anode and cathode) was applied, and the output current was recorded. We took the average current multiplied by the applied voltage to calculate the power.

$$\text{Electric Power} = \text{Current} \times \text{Voltage} \quad (\text{Eq. S3})$$

Plasma activation of water in the H-cell (small scale). Ground-state nitrogen molecules exhibit high ionization potential making it intrinsically unreactive from a thermodynamic standpoint. Still, plasma activation provides avenues for the conversion of highly stable nitrogen molecules into easier to breakdown intermediaries (NO_x). Plasma can be categorized into thermal and non-thermal plasmas (NTP). Thermal plasmas exhibit equilibrium between electrons and bulk gas temperatures (typically higher than 5 x 10³ K). Meanwhile, in NTP such equilibrium is not established; thus, the temperature of the electrons can be several orders of magnitude higher than ambient. NTP is less energy-intensive than thermal plasmas, and still possess electrons with high translational energies required to overcome the stability of the N₂ molecule via electronic structure transitions, which makes NTP a suitable choice for the process.

The design of the plasma-system, along with the input voltage, frequency, time, gas type and flow rate, liquid type (i.e. electrolyte/water) and flow rate all have a significant impact on the quantity of NO_x, the energy efficiencies of the species produced (NO_x produced/power input) as well as the ratio of nitrate to nitrite.

For the batch electrochemical tests, a custom plasma bubbler was used in an H-cell and connected to the plasma generator ('Leap 100' from *PlasmaLeap Technologies*). The optimized plasma generator parameters used a voltage of 100V, duty of 83μs, discharge frequency of 600Hz and resonance frequency of 60Hz. Dry air (Coregas, dry air) was introduced from the top of the plasma bubbler at 20 mL/min to generate PAW. The plasma activation was performed for 0.5 h to achieve a NO_x concentration of ~ 4mM in 100 mL water. This concentration range was selected based on our study on maximizing the ammonia production rate and FE using salts (Please refer to Section [Electrochemical optimization](#)).

Plasma electrical and optical measurements. A digital oscilloscope (DS6104, Rigol) was employed to record both the sinusoidal voltage and current waveform via a high voltage probe (PVM-6, North Star) and a current probe (4100, Pearson), respectively. The time-averaged discharge power (P) was calculated from the measured discharge voltage and current with Equation 4. The electrical parameters across various reactor configurations are presented in Table S2.

$$P = f \int_{t_0}^{t_0+T} u(t)i(t) dt \text{ (Eq. S4)}$$

Optical Emission Spectra (OES) were recorded using a spectrometer (SR-500i-A-R, Andor Shamrock), with a grating groove of 300 lines mm⁻¹ and exposure time of 20 ms. OES spectra were recorded in-situ for both the spark and glow discharges. For the glow discharge, the probe was located above spark discharge to minimize any interference from the spark.

Supplementary Text

Physical characterization

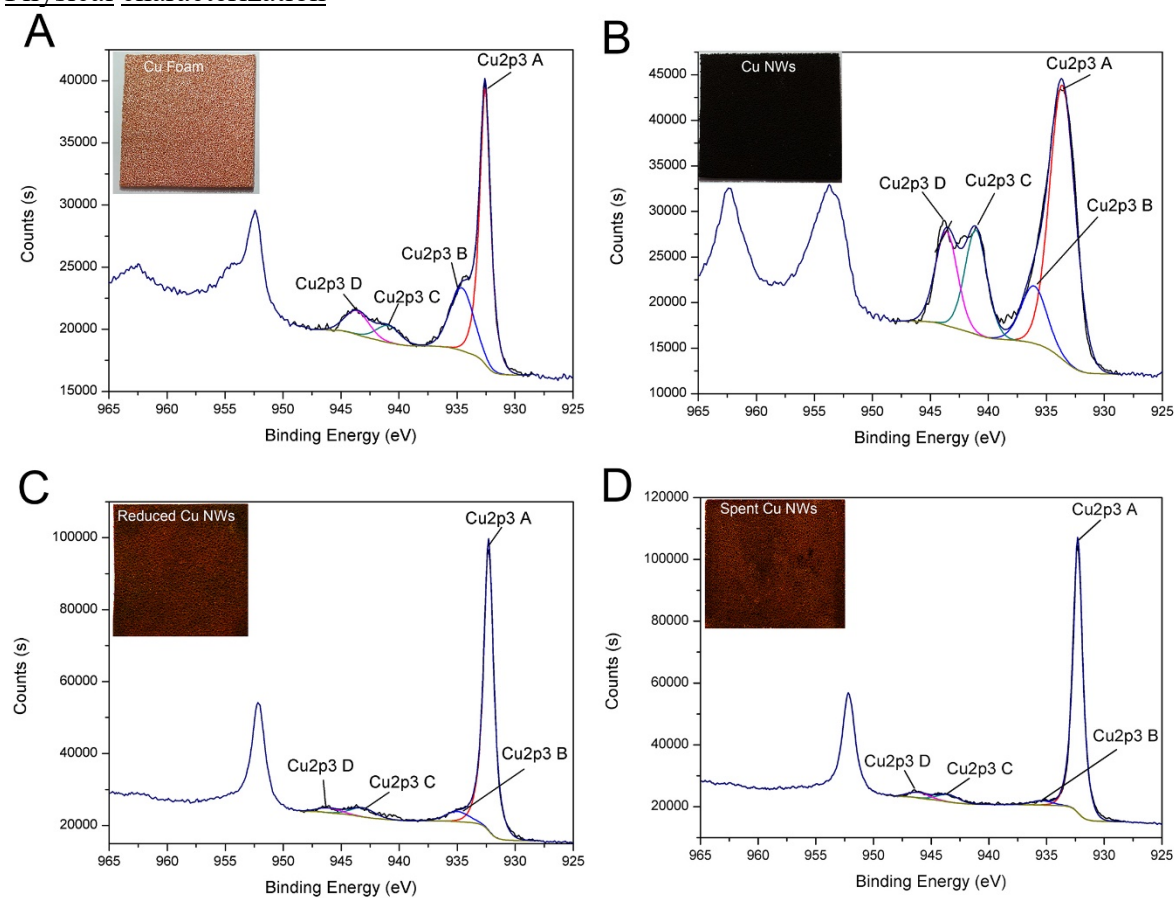


Figure S1. XPS of the Cu₂p of the electrodes: (A) Cu foam; (B) Cu NWs; (C) Reduced Cu NWs (after electroreduction) and (D) Spent Cu NWs (after reaction). Digital images of the actual 3*3 cm electrodes are shown as the inset.

To probe the active sites responsible for eNRR, we carried out XPS analysis on the as-prepared and post-reaction Cu NWs electrodes to investigate any variation in the surface chemical state of the electrode owing from the negative bias applied.

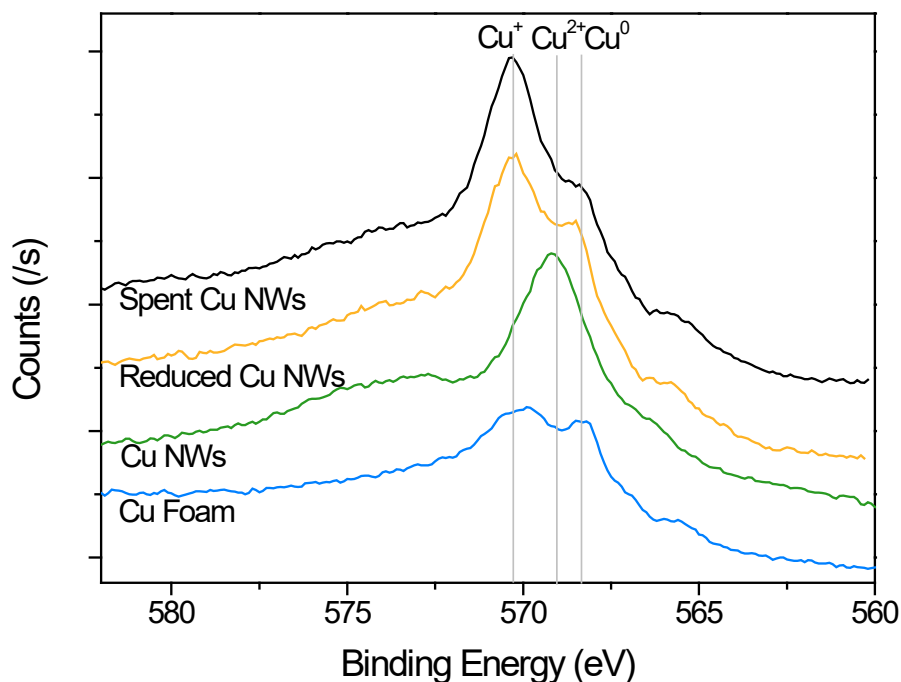


Figure S2. XPS Cu LMM spectra of Cu foam, as-prepared Cu NWs, reduced Cu NWs (after electroreduction) and (D) spent Cu NWs (after reaction). The peaks attributed to metallic Cu, CuO, and Cu₂O are at ~568.4 eV, ~569.1 eV, and ~570.3 eV, respectively.

To further understand the role of Cu oxidation state, the Cu LMM spectra was studied, as shown in **Figure S2**. From **Figure S1**, we reveal that the Cu²⁺ species are reduced to Cu⁺/Cu⁰ (indicated by the peak shift to 932.6 eV). This result is supported by the Cu LMM spectra (**Figure S2**), which clearly indicates the Cu Foam surface is comprised of a mixture of metallic Cu along with partially oxidized Cu species, likely due to the surface oxidation of the Foam. The surface of the as-prepared Cu NWs can be concluded to be CuO (as evidenced by the peak at ~569.1 eV. This is consistent with the Cu2p results, indicated the surface of the nanowires comprises of mostly of CuO species, evident from the high-resolution Cu 2p_{3/2} spectra which show a large peak at binding energy 933.7 eV which is ascribed to Cu²⁺. The reduced Cu NWs (all electrodes were electrochemically reduced prior to reaction), indicate that the surface of the Cu NWs electrode was comprised of Cu₂O.

In the ammonia production, our observed improved catalytic activity and FE of Cu NWs electrode (compared to background Cu foam and Cu foil) can be ascribed to a combination of: (i) formation of improved NRR active sites (Cu/Cu⁺) on Cu NWs, (ii) increased number of active sites and lastly (iii) enhanced mass transport allowing facile exposure to reactants and dissipation of products. The XPS characterisation of the electrodes before and after the reaction (**Figure S2**), confirmed that the Cu NWs composed of Cu/Cu⁺ species. These Cu/Cu⁺ sites facilitate faster electron transfer to nitrate reactant, enabling the formation of *NOH reactants and suppress HER, as evidenced by our result and previous theoretical calculations [1]. As such, the formation of these sites in Cu NWs compared to Cu foam and foil can explain the improved NH₃ selectivity of the electrode.

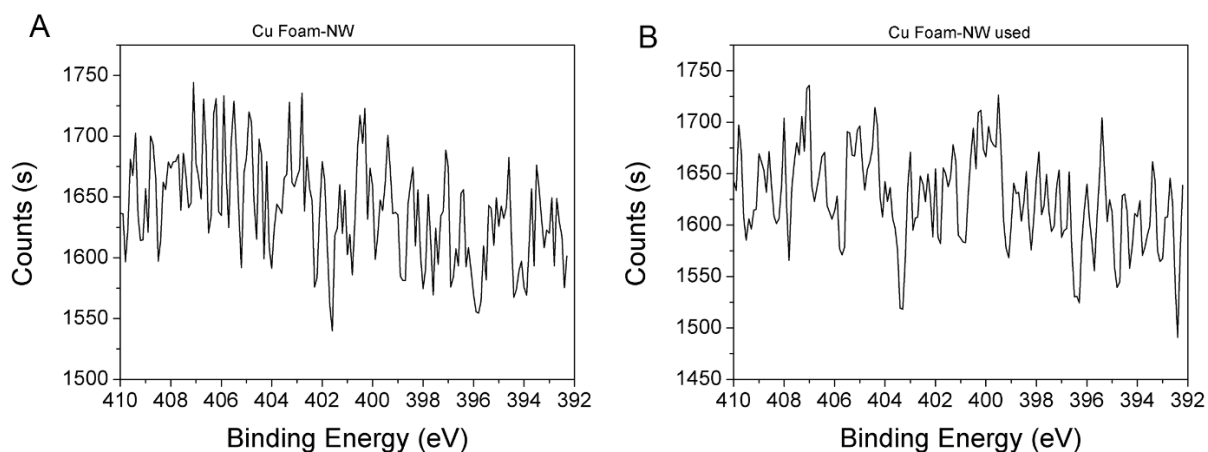


Figure S3. XPS of the N1s of the (A) as prepared Cu NWs electrode and (B) spent Cu NWs after the electrocatalytic tests (no peak was detected).

Figure S3, showing that at the N1s spectra no peak was detected, which clearly indicates that there was no nitrogen attachment to the surface of the post-reaction Cu NWs electrode. This indicates that the Cu NWs catalyst did not suffer from poisoning by the reactant NO_x species and supports the stability of the catalyst.

As the working electrode, copper has good stability in the pH and potentials that were used in this study (Pourbaix Diagrams for Copper, Ref: J. Electrochem. Soc. 144, 3476). To provide insights into the stability of the electrode in the presence of NO_3^- and NO_2^- , ICP-OES was carried out with the electrolyte after a bulk electrolysis. The ICP result reveals minor dissolution of the electrode during the reaction, indicating its stability during the reaction. In addition, SEM imaging of electrode after different electrolysis duration was carried out. shows SEM of used electrodes electrode after different electrolysis duration at two different magnifications. The images reveal an almost unchanged morphology, supporting the electrode stability.

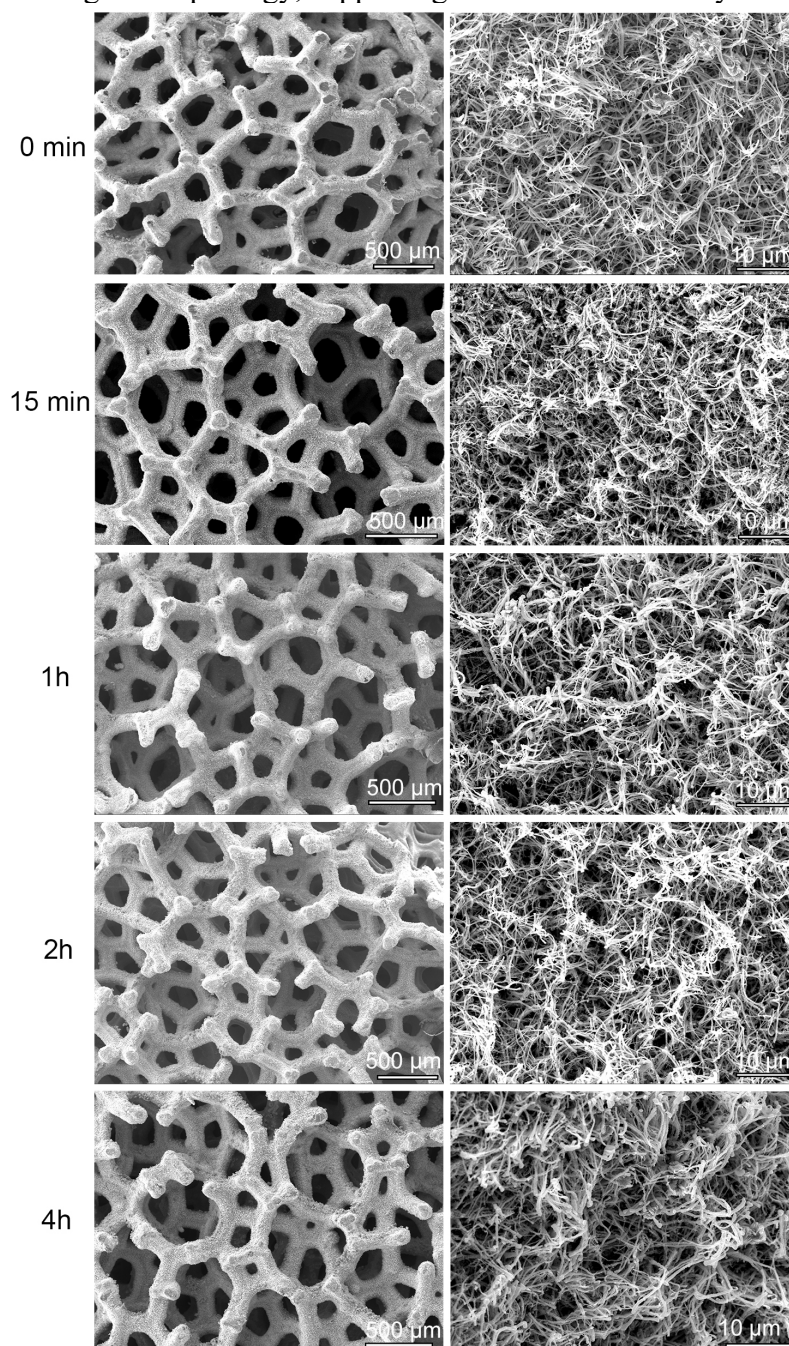


Figure S4. SEM micrographs of Cu NWs electrode after different electrolysis duration at two different magnifications.

Calibration curves

To quantify the concentration of ammonia and nitrite throughout the study, UV-Vis was utilized. **Figure S5** and **Figure S6** display the (A) UV-Vis spectra and (B) corresponding calibration curves for the $(\text{NH}_4)_2\text{SO}_4$ standard solutions and NaNO_2 , respectively.

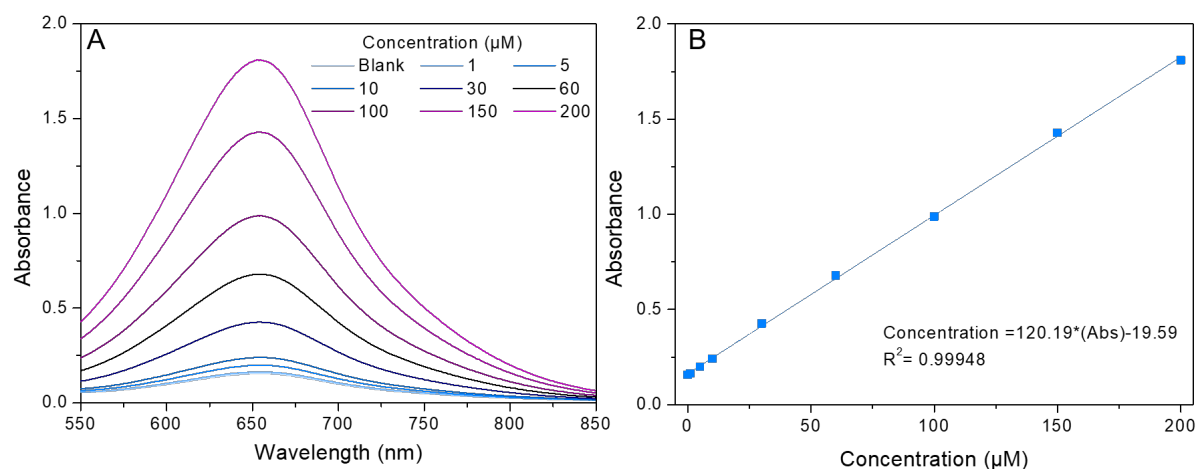


Figure S5. (A) UV-Visible absorption spectra of indophenol blue formed from the $(\text{NH}_4)_2\text{SO}_4$ standard solutions; (B) Ammonia – indophenol blue absorbance (655 nm) calibration plot used in this study.

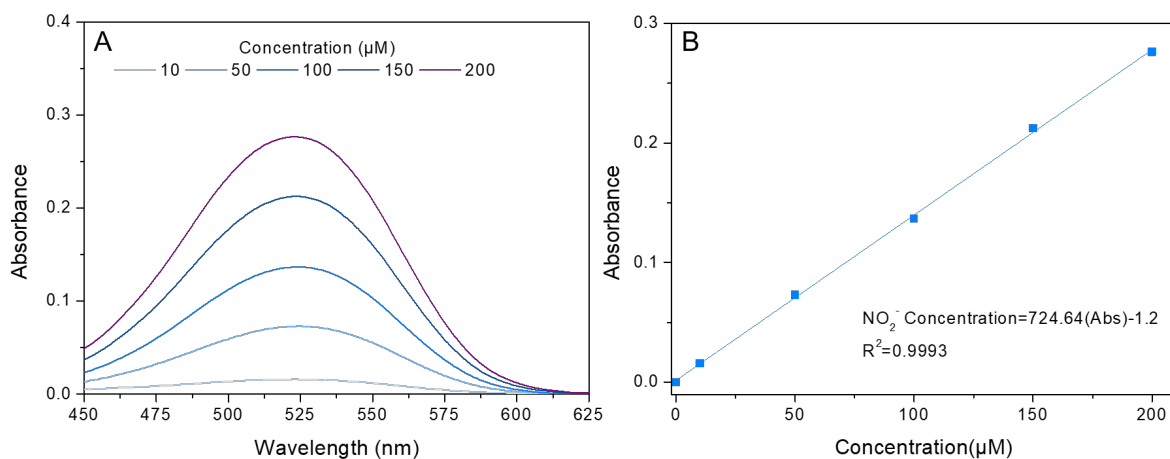


Figure S6. (A) UV-Visible absorption spectra standard solutions with different concentrations of NaNO_2 ; (B) Absorbance (525nm) calibration plot used in this study.

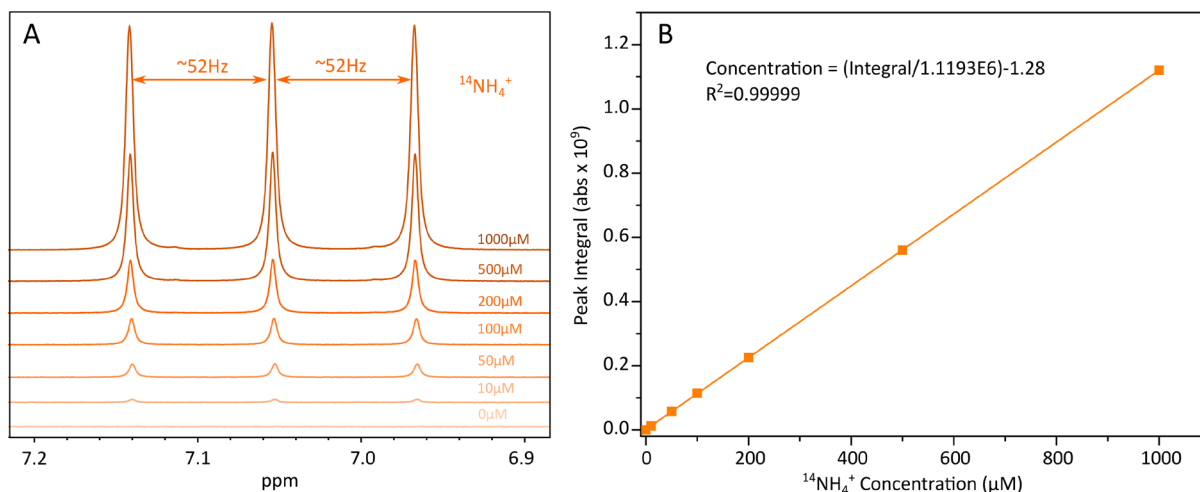


Figure S7. (A) NMR spectra of the standard solutions with different concentrations of $(^{14}\text{NH}_4)_2\text{SO}_4$. (B) Calibration curves for the $^{14}\text{NH}_4^+$.

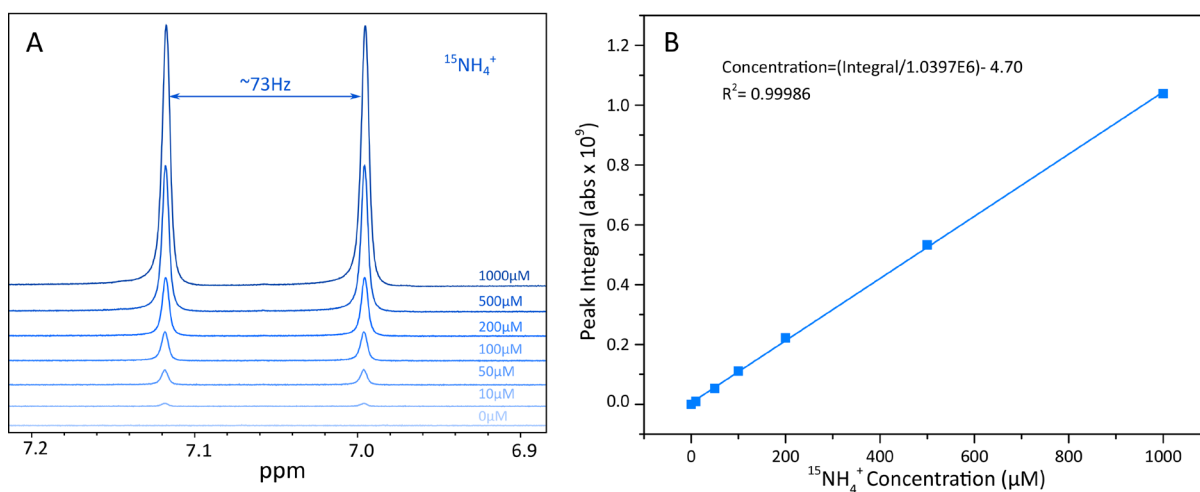


Figure S8. (A) NMR spectra of the standard solutions with different concentrations of $(^{15}\text{NH}_4)_2\text{SO}_4$. (B) Calibration curves for the $^{15}\text{NH}_4^+$.

Background determination

Table S1. List of the performed control and background determination experiments

Control No.	Electrode	Solutions/Electrolyte	Gas purge	Time/E (V vs RHE)	NH ₃ detected (μ M)
1	n.a.	Milli-Q water	None	No applied potential	Not detected
2	n.a.	10mM H ₂ SO ₄	None	No applied potential	LOD
3	n.a.	10mM H ₂ SO ₄	Ar	No applied potential	Not detected
4	n.a.	10mM H ₂ SO ₄	N ₂	No applied potential	Not detected
5	n.a.	PAW (H-cell)	Plasma activated air	No applied potential	~7
6	n.a.	PAW (column bubbler)	Plasma activated air	No applied potential	Not detected
7	Cu NWs	10mM H ₂ SO ₄	None	15 min/-0.5V	Not detected

To investigate the background of NH₃ and NO_x in the used electrolytes, PAW, solutions and electrodes, the following control experiments have been carried out. These experiments are outlined in **Table S1** and were undertaken to evaluate the following: (1) determination of ammonia concentration in Milli-Q water, (2) determination of ammonia concentration in the background electrolyte without gas purging, (3) determination of ammonia concentration in the background electrolyte after purging with Ar for 0.5 h, (4) determination of ammonia concentration in the background electrolyte after purging N₂ for 0.5 h, (5) determination of ammonia concentration in plasma-activated water (PAW) from H-cell design, (6) determination of ammonia concentration in PAW from column bubbler design and (7) determination of ammonia concentration in the electrochemical cell containing background electrolyte and electrodes (applied potential of -0.5 V vs. RHE for 0.25 h). The results from these control tests are displayed in **Figure S9**.

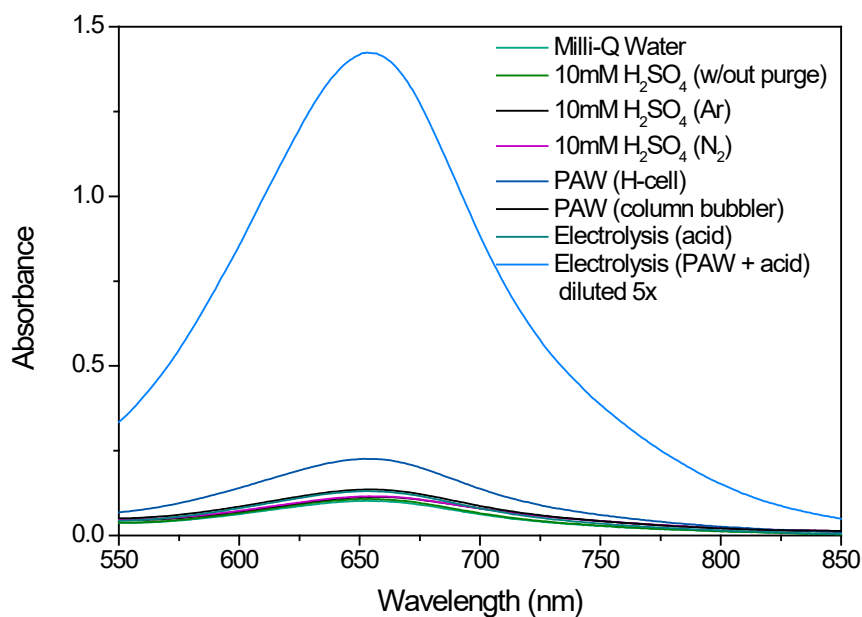


Figure S9. UV-Visible absorption spectra of indophenol blue formed from the NH_3 , providing results for the control tests outlined in **Table S1**.

Using a H-cell, we observed a small quantity of ammonia, at the rate of 0.21 nmol s^{-1} , during the plasma activation. However, with the plasma column bubbler, no ammonia was detected in the electrolyte as it was designed to be specific toward the production of NO_x . In the case of the electrolysis of PAW, we obtained the significant production rate of $45 \text{ nmol cm}^{-2}\text{s}^{-1}$. Moreover, the measured ammonia in the background electrolyte, as well as the other controls, was in the range of the limit of detection. This result clearly indicates that environmental contamination is not contributing to the ammonia production rate reported in this work.

Electrochemical optimization

The first step toward the optimization of the electrocatalytic conversion of NO_x to ammonia was performed using nitrate (KNO_3) and nitrite (NaNO_2) salts as the NO_x source, and Cu foil (1cm x 1cm) as the cathode, Pt wire as the anode and Ag/AgCl (*sat.* KCl) as the reference electrode in a custom-designed H-cell (**Figure 2B**). The cation in the NO_x salts is assumed not to play a significant role in the performance (hence KNO_3 and NaNO_2 salts were used as the NO_x source).

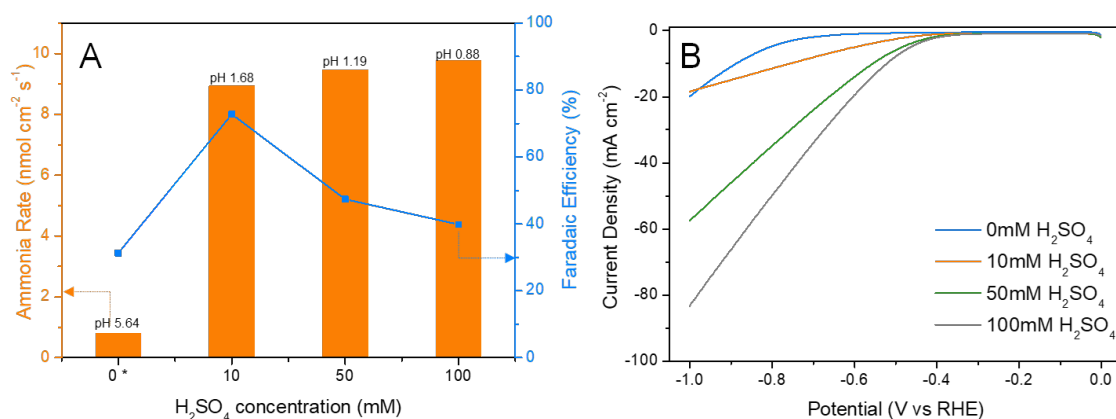


Figure S10. Optimization of the electrolyte *via* adjusting the pH of electrolyte using sulfuric acid with 1mM NaNO_2 as the NO_x source. (A) Ammonia production rates and the corresponding Faradaic Efficiencies in different sulfuric acid concentrations at -0.5V vs RHE for 15 min and using Cu foil (1cm x 1cm) as the catalyst; (B) Representative linear sweep voltammetry (LSV, 0V to -1V) of electrolyte containing various concentrations of sulfuric acid. 0.5M Na_2SO_4 was added to adjust conductivity when there was no acid in the electrolyte.

In acidic media, the reaction proceeds, as shown in Equations S5-S8 below. The reaction competes with the hydrogen evolution reaction (HER), Equation S8[2]. Transition metals, such as Cu, are beneficial for ammonia production as they are able to suppress the competing hydrogen evolution reaction (HER). Generally, the potentials applied in aqueous phase nitrate and nitrite reduction reactions are above the onset overpotential for HER. Given that the reaction kinetics for HER is faster compared to NRR (owing to the requirement of two-electron transfer to form H_2 compared to 8 electron transfer to generate NH_3 from nitrates), HER will dominate over NRR on a catalyst that is active for both reactions. As such, through designing Cu/Cu^+ active sites within our Cu NWs electrode, we were able to suppress hydrogen evolution and as a result, attain prominent selectivity and yield for NH_3 generation.



Theoretical calculation from the literature [1] suggested that firstly NO_3^- adsorbs to the catalyst active sites to form $^*\text{NO}_3$ with a total decrease in energy. Next spontaneously, the N–O bond of $^*\text{NO}_3$ cleaved step by step to generate $^*\text{NO}_2$ and $^*\text{NO}$. Subsequently, the

hydrogenation step of *NO to produce *NOH occurs, the *NOH hydrogenated to produce *NH₂OH and then transformed into *NH₃. Ultimately, *NH₃ desorbed from the catalyst.

Whilst H⁺ is required to facilitate the reaction, a high concentration of H⁺ may result in occurrence of HER. In our experiment, when H⁺ was not available in the electrolyte, both FE and ammonia yield rate was very low (> 30% and 1 nmol cm⁻²s⁻¹, respectively). The addition of acid (10mM H₂SO₄) in the electrolyte resulted in a significant increase in the ammonia production rate and FE, from 0.81 to 8.94 nmolcm⁻²s⁻¹ and from 31% to 73%, respectively. However, a further increase in the acid concentration did not positively impact the ammonia production while the FE dropped significantly as HER became more competitive.

In order to perform NO_x reduction to NH₃, a potential window that is higher than the theoretical potential for nitrate and nitrite reduction to NH₃ was used (0.2V to -0.7V vs RHE). This potential is more negative compared to water splitting potential (see equation S5-8). This is because at low potentials (closer to the theoretical potential), the energy applied is not high enough to overcome sluggish reaction kinetics and system impedance and therefore the yields are very low. Given that source of ammonia generated during electrochemical reactions is under scrutiny owing to possible contaminations, we limit our testing in the range where we can conclusively demonstrate the yield to be from NO_x reduction.

To further assess the role of acid, we performed a bulk electrolysis experiment where pH and ammonia amount were measured (50 mL plasma activated water containing 10mM H₂SO₄ and electrolysis at -0.5 V vs RHE for 1.5h). In this experiment, the pH changed slightly from 1.29 to 1.5 while 256 μmol of NH₄⁺ was generated. Considering the stoichiometric equation S5, the total amount of protons required during this bulk electrolysis is 1280 μmol, far exceeding the protons supplied by the acid in the electrolyte (total of 500 μmol was added). From this experiment, the majority of the protons are being supplied from water, which acts as a reactant and acid as a chemical bias.

Therefore, in this study, 10mM H₂SO₄ was used as the background electrolyte which (a) increases the conductivity of the electrochemical system to minimize energy losses caused by the resistance; (b) supports synthesis of ammonium sulphate (NH₄)₂SO₄ which is soluble in water and can be used directly as a fertilizer.

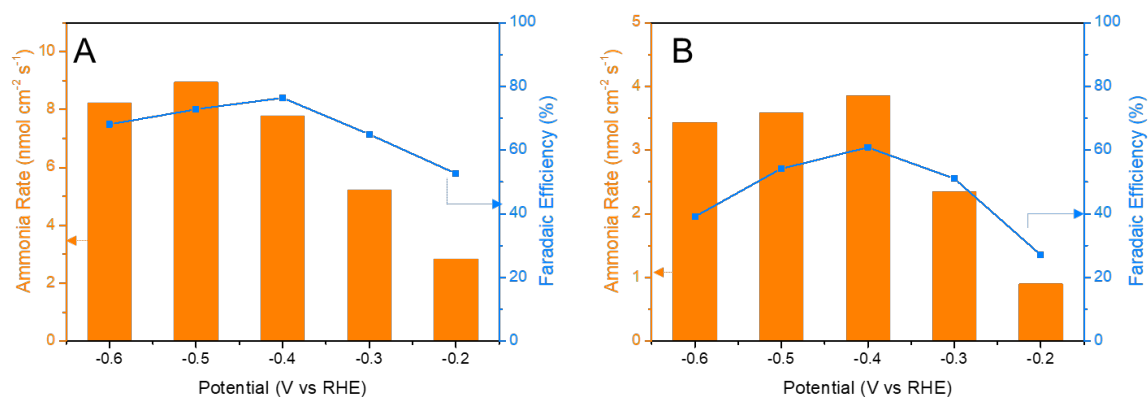


Figure S11. Nitrite and nitrate salts potentials study. Ammonia production rate and the corresponding FE of (A) 1mM NaNO₂ solution and (B) 1mM KNO₃ solution under different potentials from -0.2V to -0.6V.

When nitrite was used as the reactant, ammonia production rate increased with more negative potentials, and the rate reaches its maximum at -0.5V with FE of about 73%. While for nitrate, its maximum production rate ($\sim 3.8 \text{ nmol cm}^{-2}\text{s}^{-1}$) and FE ($\sim 60\%$) occurred at -0.4V. Beyond the optimal potential, both rate and FE start to decrease due to a possible occurrence of HER.

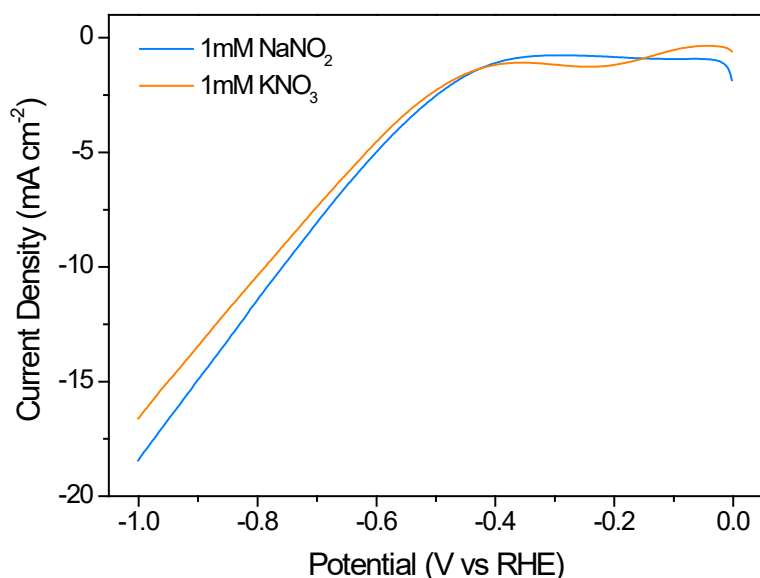
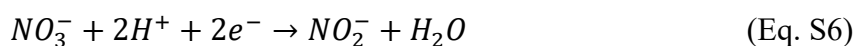


Figure S12. LSV curves (scan rate of 5mV/s) of 1mM NaNO₂ and 1mM KNO₃ solutions from 0V to -0.8V

Figure S12 compares the LSV curves of nitrate and nitrite salts in 10 mM H₂SO₄. The reduction of nitrate to nitrite (Eq. S6) is evidenced by a peak occurred at around -0.25V on the LSV curve of the nitrate solution (1 mM KNO₃).



This result indicates that at lower potentials, nitrate is more favourable to be converted to nitrite rather than ammonia (which is in agreement with the literature [3]). To investigate, a 15min electrolysis experiment was conducted in 50 mL of 1 mM KNO₃ solution at -0.3V. We found that 0.7 μmol of ammonia was produced, while 1.17 μmol of nitrite was produced at this potential. On the other hand, when the experiment was performed at -0.5V, 1.64 μmol ammonia and 0.66 μmol nitrite were produced.

During NO_x reduction, it is established that NO₃⁻ is first adsorbed to the surface of the electrode to form *NO₃ and the N-O bond is then spontaneously cleaved stepwise producing *NO₂ and *NO. Next, the hydrogenation of *NO to form *NOH occurs. Successively, the *NOH hydrogenated to form *NH₂OH and then transformed into *NH₃. Finally, *NH₃ desorbed from the catalyst. In this process, we observed a portion of the *NO₂ desorbed into the solution as NO₂⁻, hence the observed lower FE of ammonia conversion at the lower potentials (See Figure 2F in the main text, between 0.2 to -0.2 V). At higher potentials, however, the conversion rate of both nitrate and nitrite to ammonia is very high; therefore, the produced nitrite also converted to ammonia at the vicinity of the catalyst.

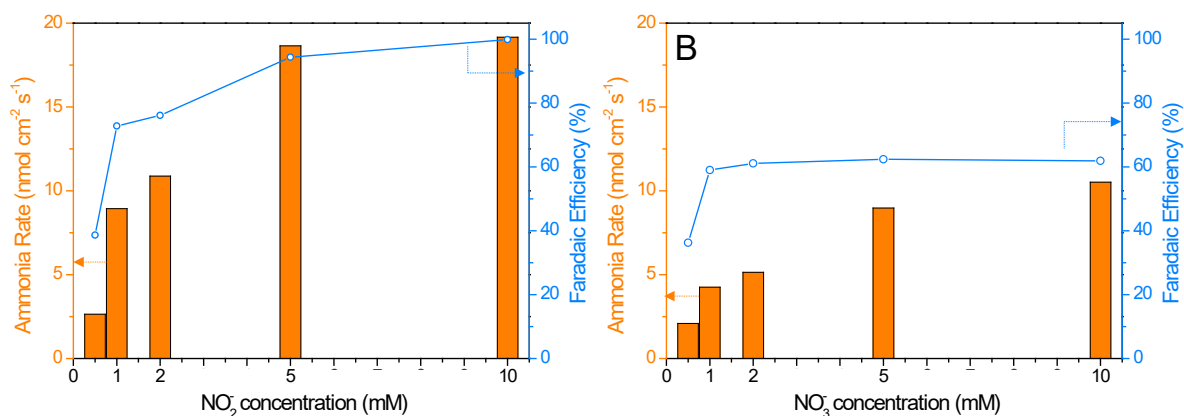


Figure S13. NO_x (nitrite and nitrate) concentration study to increase rate and FE. Ammonia production rate and the corresponding FE in different concentrations of (A) NaNO₂ and (B) KNO₃ solutions under $-0.5V$ vs RHE for 15 minutes.

To investigate the effect of NO_x concentration on the ammonia production rate and FE, a range of concentrations of nitrite and nitrate salts were tested (**Figure S13**). In the case of NO₂⁻ salt, much higher production rates and FEs were observed compared to NO₃⁻ salt. Please note, the FE of the conversion of NO₂⁻ to ammonia can reach 100% while the FE of NO₃⁻ stays at around 60%. The lower FE when NO₃⁻ was used can be ascribed to some charge loss arising from the conversion to NO₃⁻ to NO₂⁻ species instead of ammonia. However, both NO₃⁻ and NO₂⁻ are converted to ammonia in the end, when the experiment continues to consume all the available NO_x (FE of 100%). For both nitrite and nitrate, ammonia production rates and FE increased significantly when the concentration reached at ~1 mM. This graph was our guide to set the duration of the plasma activation (achieving NO_x concentration of >1 mM) to maximize the ammonia production rate and FE.

Catalyst surface area

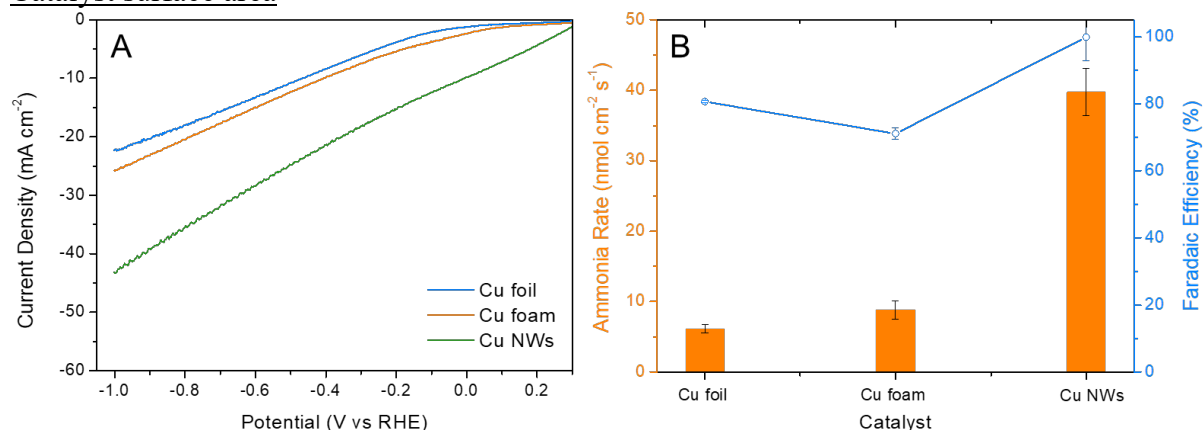


Figure S14. (A) LSV curves of copper catalysts with different porosity (Cu foil, Cu foam and Cu NWs) in PAW electrolyte; (B) ammonia production rates and FE using these catalysts.

To compare copper-based catalyst performance as a function of available surface area, control experiments were performed with Cu foil and Cu foam. Cu NWs electrode facilitated a very high current density (j), -45 mA cm^{-2} at -1V , compared to -22 mA cm^{-2} for Cu foil and -26 mA cm^{-2} for Cu foam. Cu NWs also facilitated a much higher catalytic activity for ammonia synthesis with a production rate of $40 \pm 3.3 \text{ nmol cm}^{-2} \text{ s}^{-1}$ and FE of $100 \pm 7\%$. At the same time, Cu foil only provided ammonia production rate of $6.1 \pm 0.6 \text{ nmol cm}^{-2} \text{ s}^{-1}$ with FE of $80.6 \pm 0.3\%$ and Cu foam had a rate of $8.8 \pm 1.3 \text{ nmol cm}^{-2} \text{ s}^{-1}$ with FE of $71.1 \pm 1.7\%$.

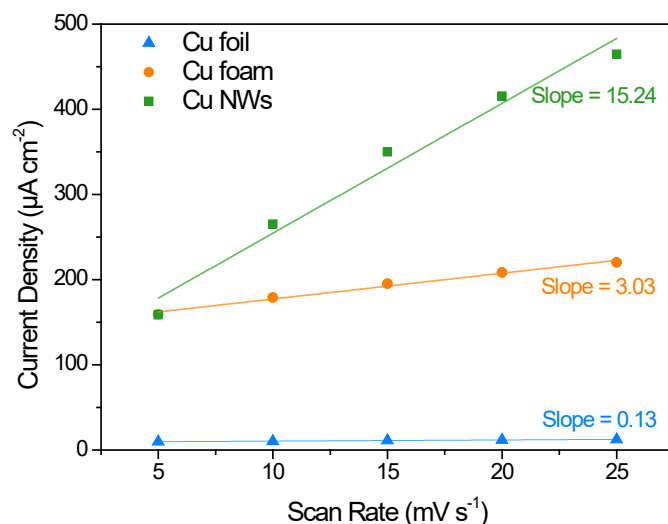


Figure S15. Electrochemically active surface area (ECSA) comparison of various forms of copper catalysts (Cu foil, Cu foam and Cu NWs in 0.5M Na₂SO₄ solution) used in this study.

In the case of Cu foil and Cu foam, non-Faradaic charging currents are measured in the potential range of 0.5V and 0.55V vs RHE and for Cu NWs, the potential range is 0.25V to 0.30V vs RHE. The scan rate is varied between 5, 10, 15, 20 and 25 mV/s and the anodic (positive) and cathodic (negative) current densities are obtained from the double layer charge/discharge curves at 0.525V vs RHE for Cu foil and Cu foam and 0.275V vs RHE for Cu NWs. The double-layer capacitance was then calculated by averaging the absolute values of cathodic and anodic current densities and take the slopes of the linear fits. The slopes obtained with Cu foil, Cu foam and Cu NWs are 0.13mF/cm², 3.03mF/cm² and 15.24mF/cm² respectively, indicating that the fabricated catalyst Cu NWs has much larger electrochemical active surface area compared to the commercial Cu foil and Cu foam.

The enhanced active surface area for the Cu NWs electrode compared to Cu foam and foil, indicating a greater number of active sites on the electrode, which can help explain the observed higher j of the electrode (**Figure S14**). As a result, the three-dimensional porous structure with abundant number of Cu/Cu⁺ active sites enable the Cu NWs electrode to display prominent activity.

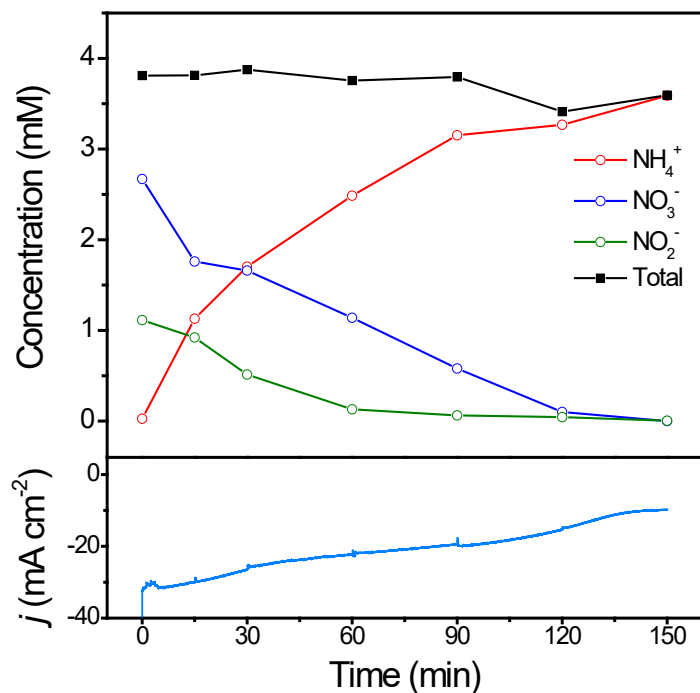


Figure S16. Time-dependent concentration of NO₃⁻, NO₂⁻, and ammonium during 2.5h electrolysis at -0.5 V vs RHE with Cu NWs with sampling of nitrite, nitrate, and ammonia along with the chronoamperometric *i*-*t* curve.

With an extended reaction time of 2.5h (**Figure S16**), both NO₃⁻ and NO₂⁻ species were completely exhausted (from 2.7 mM and 1 mM, respectively). On the other hand, ammonia concentration increases from 0 mM to 3.5 mM over the same period. A slightly lower final concentration of ammonia compared to initial concentration of NO_x was obtained (3.5 vs 3.7 mM). This reduction can be attributed to the loss of a small amount of NO_x and ammonia due to sampling. The chronoamperometric *i*-*t* curve displays a consistently declining *j* which indicates the consumption of the reactants during this 2.5h.

Scaled-up plasma system development

Plasma reactors, discharge schemes and configurations

Five reactor design configurations using underwater plasma bubbles were tested. Photographs of plasma bubble column reactors design configurations are shown in **Figure S17**, were: (a) single reactor glow discharge (SRGD); (b) single reactor spark discharge (SRSD); (c) single reactor glow and spark discharge (SRGSD); (d) double reactor glow and spark discharge (DRGSD); and (e) DRGSD with Raschig rings. Plasma bubble column reactors were capable of dual-discharge mode operation (glow and spark discharge). To achieve the former, the high voltage electrode was sheathed with borosilicate. The latter incorporated a sharpened high voltage electrode with a 1 cm protrusion which induced a spark extending longitudinally towards the bubbles. Meanwhile, combinative discharge reactors coupled both these concepts in a single unit. In configurations involving the single reactor, the circuit was completed via connecting the negative terminal to a copper electrode (40x80mm) connected to the outside wall of the reactor vessel. For the double-reactor configurations a second reactor was connected to the negative terminal. In all cases the water volume was part of the circuit. Plasma reactors were fabricated using a quartz tube with one end sealed and 12 laser-drilled holes with a diameter of 200 μ m located radially 5 mm above the sealed base. Stainless steel rod was used as the reactor electrode inserted concentrically into the quartz tube. A tee fitting was connected to the quartz tube to position the electrodes. Instrument grade air was injected as the feed gas at a flow rate of 2 L/min in each reactor via a mass flow controller. Reactors were powered by plasma generator ('Leap100', *PlasmaLeap Technologies*) capable of yielding voltage output of 0-80 kV (peak-to-peak), discharge power of up to 700 W, and a discharge frequency range of 100 Hz–3000 Hz. For all experiments, power was provided in form of batches of sinusoidal pulses with a lag time between each batch. Resonance frequency of the pulse was set at 60 kHz while discharge frequency of each batch of pulses was 300 Hz (duty cycle of 103 μ s). We employed an AC sinusoidal waveform with periodic gaps between discharges. Compared to DC plasmas, AC waveform is considered more efficient, inexpensive, and reliable for longer operations. This is because of higher excited state active species at similar powers (in some cases 5 times higher [4] due to less energy dissipation into heat at the electrodes in aqueous environments).

Temperature measurements before and after plasma-activation were undertaken to determine the impact of plasma-activation on system temperature. For the process, there was a negligible change in the temperature in the plasma activated water, 1-2 $^{\circ}$ C, after 10 minutes of plasma exposure. In a typical experiment the water temperature changed from around 18-20 $^{\circ}$ C to 20-22 $^{\circ}$ C.

In the case of the shape of the tip of the plasma generator, although parameters such as the angle, size, shape and area of the sharpened tip could be important, considering the size of the volume of liquid and the reactor, the difference in the results would likely be fairly negligible. In our experiment, we found the sharpened point at the electrode tip focusses the electric field on creating a single plasma arc in the centre of the tube which then splits into a streamer into each hole/bubble. Alternative shapes such as a rounded or flat tip was not able to achieve the same, consistent plasma discharge occurring into each of the 12 holes compared to a sharpened tip. Additionally, a flat electrode tip leads to favouring discharge through a specific hole or discharging simply into the sidewalls of the tube (as a flat tip would be closer to the sidewalls of the tubing) which would not be conducive to generating active species.

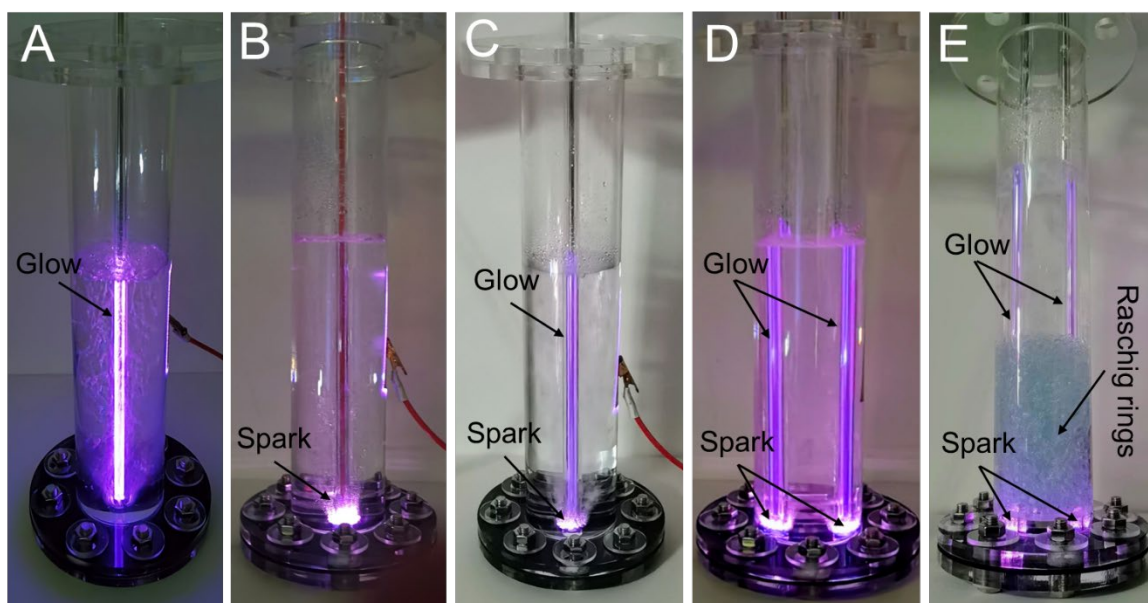


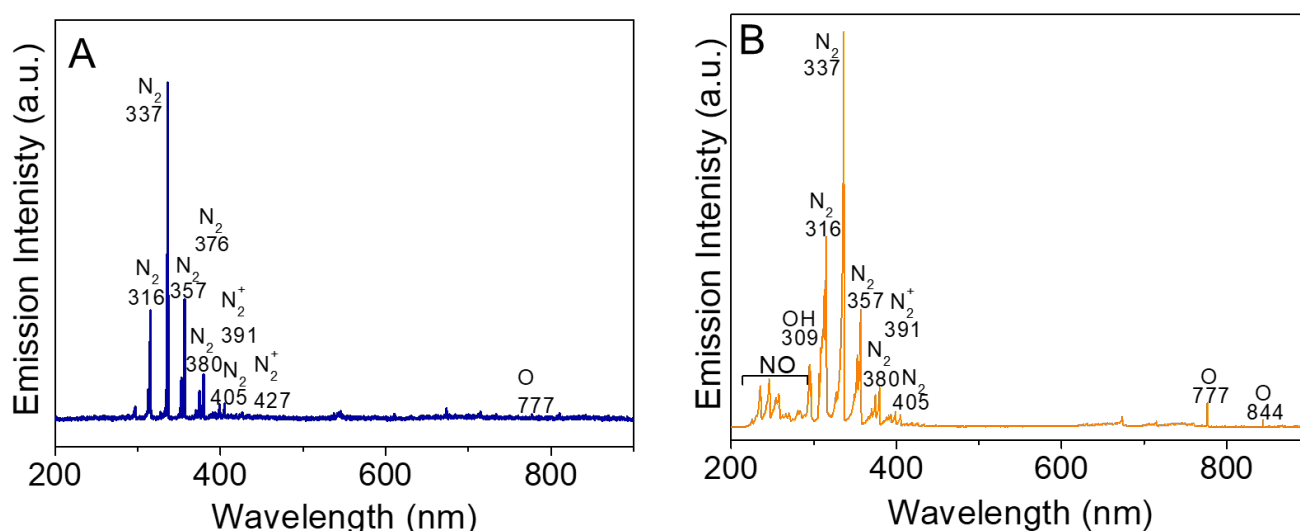
Figure S17. Photographs of plasma bubble column reactors design configurations: (A) single reactor glow discharge (SRGD); (B) single reactor spark discharge (SRSD); (C) single reactor glow and spark discharge (SRGSD); (D) double reactor glow and spark discharge (DRGSD); and (E) DRGSD with Raschig rings.

Refer to Movie S1-S5 for videos showing the operation of single reactor glow discharge (SRGD, Movie S1), single reactor spark discharge (SRSD, Movie S2), single reactor glow and spark discharge (SRGSD, Movie S3), double reactor glow and spark discharge (DRGSD, Movie S4), and DRGSD with Raschig rings (Movie S5). Movie S6 shows the plasma discharge within bubbles.

Table S2. Operational conditions of plasma reactors and production rates of species

Reactors	Voltage amplitude (kV)	Current amplitude (A)	Power (W)	Operation time (min)	Mean NO ₃ ⁻ (ppm)	Mean NO ₂ ⁻ (ppm)	Conductivity (μS/cm)	pH
SRGD	12.5	0.38	7.38	10	4.6	0	37.70	4.02
SRSD	9.8	0.5	9.22	10	1.8	4.8	38.37	4.00
SRGSD	8.7	1.56	10.67	10	9.9	7	107.47	3.54
DRGSD	8.5	1.68	11.27	10	20.2	4.5	170.20	3.37
DRGSD+ Raschig rings	8.4	1.68	11.27	10	24.9	4.3	209.90	3.29

Further, polarity inversion in AC systems prompts current passing through zero at half cycle which enhances the lifetime of electrodes. The reason of using non-thermal plasma is to selectively transfer incident electric power to the electrons rather than volumetric heating of the entire gas; an energy-efficient route to formation of active species via collisions. There are reports on production of higher production of reactive radicals in the aqueous phase because of mechanical agitation and local heating caused by bursting of bubbles [5].

**Figure S18.** Optical Emission Spectra (OES) measurements representing (A) the glow discharge and (B) spark discharge.

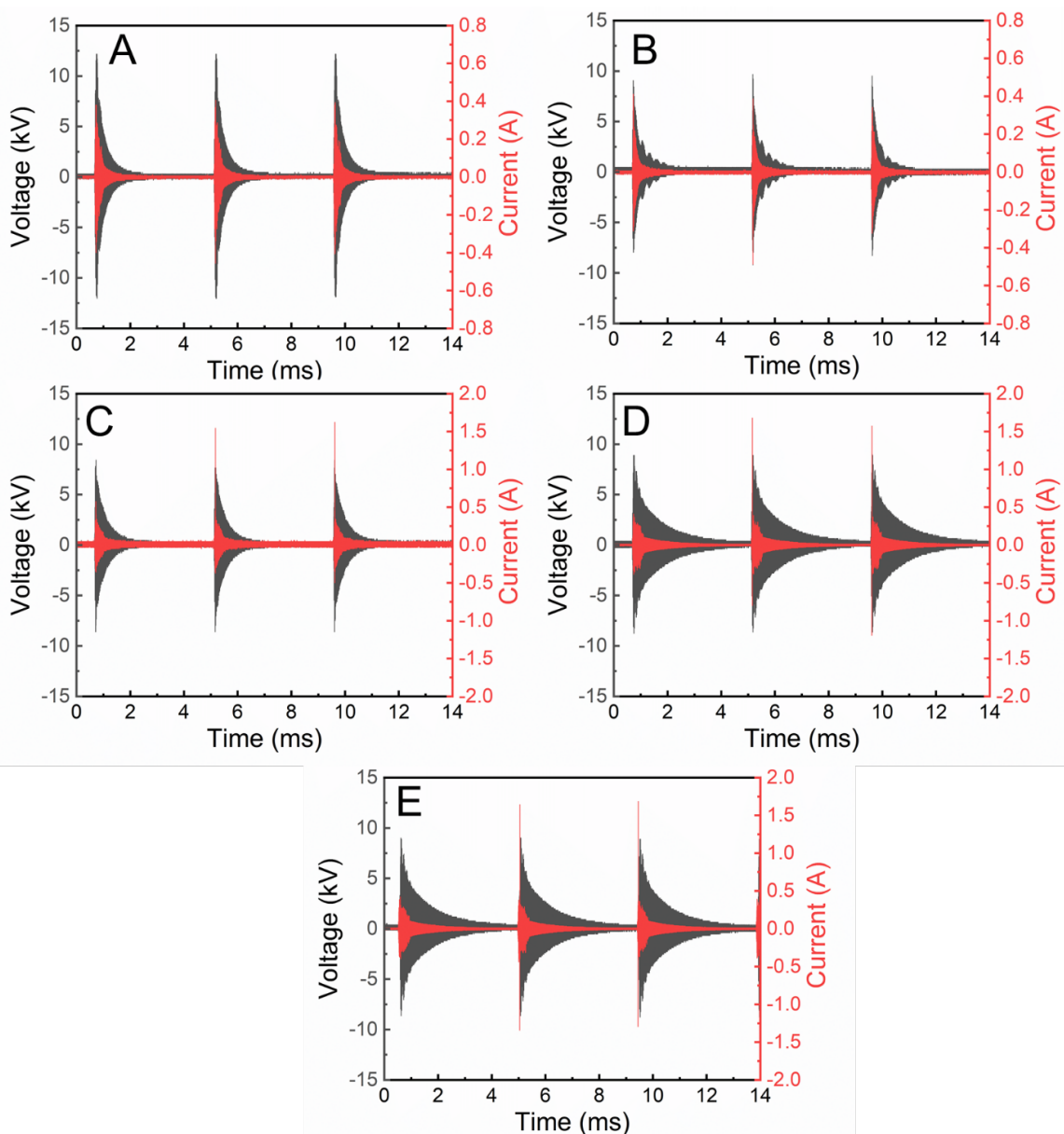


Figure S19. Electrical diagnostic data for (A) single reactor glow discharge (SRGD); (B) single reactor spark discharge (SRSD); (C) single reactor glow and spark discharge (SRGSD); (D) double reactor glow and spark discharge (DRGSD); and (E) DRGSD with Raschig rings.

Single reactor glow discharge (SRGD) was operated under a glow-only discharge scheme by applying 7.38 W power and using a dielectric barrier covering the high voltage electrode. In principle, the use of dielectric barrier limits the flow of charge enabling higher voltages at the same power, as reflected by electrical diagnostics measurements provided in Table S1. In this discharge scheme, the production of NO_3 predominated over NO_2 , which is consistent with literature. Meanwhile, the spark-only discharge scheme was dominated by NO_2 over NO_3 , and higher current to voltage ratios than the glow-only scheme and comparatively higher power (9.22 W). High intensity electric fields in the glow discharge scheme favour ozone production, which maintains an oxidative environment throughout the entire volume in the tube facilitating conversion of NO_2 to NO_3 . However, spark streamers are confined in the concentrated volume prompting formation of high energy species and back-reactions of NO_3 to NO_2 .

Plasma activation of water as function of time

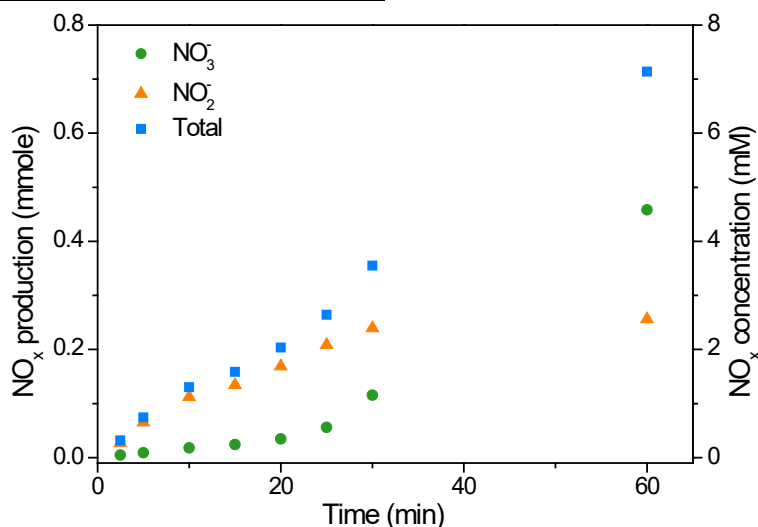


Figure S20. Time-dependent moles and concentration of plasma generated NO_3^- and NO_2^- in the H-cell containing 100 mL of water.

The concentration of NO_x was controlled by the plasma activation time under the optimized parameters (voltage of 100V, duty of $83\mu\text{s}$, discharge frequency of 600Hz and resonance frequency of 60Hz). It is shown from both **Figure S20** and **Figure S21**, the total amount of NO_x increases linearly as a function of plasma activation time. In this study, 0.5 h of plasma activation (produces $\sim 4\text{mM}$ NO_x in 100 mL of water) was selected for the electrolysis tests. This plasma activation time was selected based on our systematic study on the effect of NO_x concentration (using nitrate and nitrite salts) on the FE and production rate of ammonia (**Figure S11**).

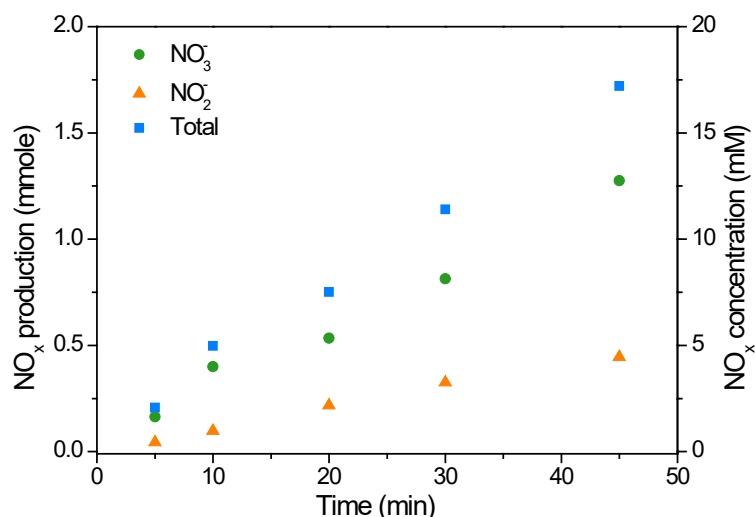


Figure S21. Time-dependent moles and concentration of plasma generated NO_3^- and NO_2^- in the column bubbler (DRGSD + Raschig rings) containing 1L of water. As shown, the total concentration of NO_x increases linearly as a function of plasma activation time.

$^{15}\text{N}_2$ labelling experiment

To confirm dinitrogen is the sole source of the ammonia production, we have undertaken quantitative ^{15}N isotopic tracer studies as a function of time and feed gases ($^{14}\text{N}_2$, $^{15}\text{N}_2$, and Ar). Using ^1H NMR technique, we could effectively quantify ammonia and distinguish $^{15}\text{NH}_4^+$ from $^{14}\text{NH}_4^+$ (**Figure S7** and **Figure S8**). Control tracer studies (including with ^{14}N and Ar) also confirms the validity of this assessment. With Ar gas as the feed, a negligible trace amounts of ammonia was detected, which did not increase as a function of time (**Figure S22A**, environmental contamination). On the other hand, $^{14}\text{N}_2$ feed produced a significant amount of ammonia, which increased steadily as a function of time (triplet in **Figure S22B**). Furthermore, $^{15}\text{NH}_4^+$ quantification was performed to prove that ammonia is produced from N_2 rather than from the reduction of ubiquitous nitrogen oxides or just contamination. The doublet at approximately 7.0 to 7.1 ppm in **Figure S22 C** confirms $^{15}\text{NH}_4^+$ was produced (from $^{15}\text{N}_2$) and steadily increased during the electrolysis (**Figure S22D**). These results validate the production of ammonia comes from the plasma-activated nitrogen feed. These results are consistent with our control studies presented in **Figure S9**, which shows that in the absence of a N_2 plasma, ammonia production was suppressed.

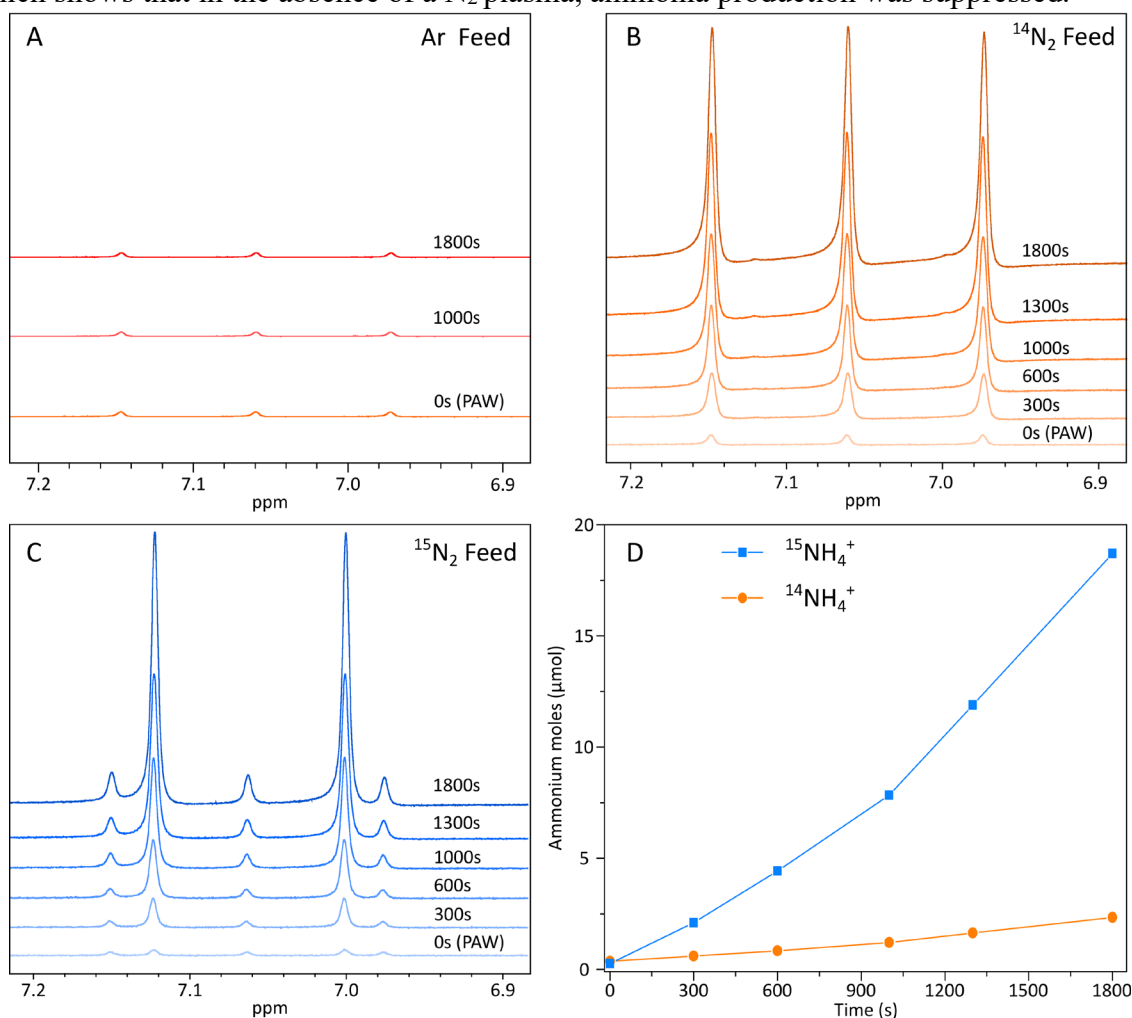
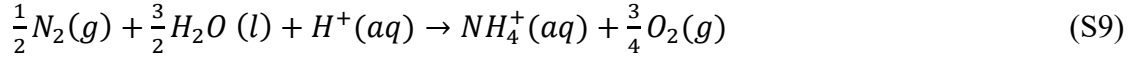


Figure S22. Ammonia ^{15}N isotopic tracer studies and ^{14}N and Ar control results. (A-C) NMR spectra showing ammonia production as a function of electrolysis time using different gas feeds. (A) Ar, (B) $^{14}\text{N}_2$, (C) $^{15}\text{N}_2$. The times indicated in each spectrum is the duration of the electrolysis before the sample collection. The scale on the y-axis of NMR spectra in (A-C) is the same. (D) $^{15}\text{NH}_4^+$ production as a function of time using $^{15}\text{N}_2$ feed. The $^{14}\text{NH}_4^+$ that was generated from ^{14}N impurities is shown for comparison.

Calculation of energy conversion efficiency

To calculate the total energy efficiency, we have calculated the required energy for ammonia synthesis from its building block then used this figure to calculate the total energy conversion efficiency as outlined below:

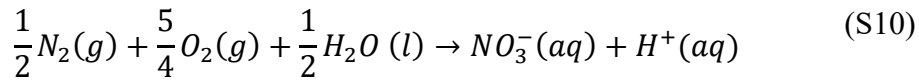
The overall system (with acid as an additive) is:



$$\Delta H^{\circ} = 296.3 \text{ kJ/mol of } NH_4^+$$

$$\Delta G^{\circ} = 276.4 \text{ kJ/mol of } NH_4^+$$

The reaction for the plasma nitrogen activation is described by Equation S10.



$$\Delta H^{\circ} = -64.5 \text{ kJ/mol of } NO_3^-$$

$$\Delta G^{\circ} = 7.3 \text{ kJ/mol of } NO_3^-$$

Chemical equation for electrochemical side



$$\Delta H^{\circ} = 360.7 \text{ kJ/mol of } NH_4^+$$

$$\Delta G^{\circ} = 269.1 \text{ kJ/mol of } NH_4^+$$

Table 3. Enthalpy (ΔH_f°) and Gibbs free energy (ΔG_f°) of the reactants and the products.

Compounds	ΔH_f° (kJ/mol)	ΔG_f° (kJ/mol)
N ₂ (g)	0	0
O ₂ (g)	0	0
H ₂ O (l)	-285.83	-237.178
H ⁺ (aq)	0	0
NO ₃ ⁻ (aq)	-207.4	-111.3
NH ₄ ⁺ (aq)	-132.5	-79.37

Energy efficiency for the hybrid system:

$$\eta = \frac{296.3}{15483.6} \times 100\% = 1.9\%$$

$$253\text{kwh/kg } NH_3 = 15483.6\text{kJ/mol}$$

Performance benchmarking

Table S4. Compilation of reported ammonia synthesis at ambient conditions

(A) Electrocatalytic benchmarking (including plasma-assisted systems)

Cathode	Anode	Conditions		Ammonia Rate		FE (%) ^a	Specific Energy Consumption (kWh/kgNH ₃)	Current Density (mA/cm ²)	Cell potential (V)	Ref.	Comments
		Electrolyte	Feed gas	nmol/cm ² s	mg/h						
Cu Nanowires	DSA®	PAW +0.01M H ₂ SO ₄	Air	42.12	23.2	87-55	253 ^d	51.6	1-1.5V	This work	With electrolyzer, 9cm ² (plasma-assisted system)
Cu Nanowires	Pt	PAW +0.01M H ₂ SO ₄	Air	45.3	2.77	100	234 ^{b,c}	33	-0.6V vs. RHE	This work	With H-cell, 1cm ² -0.9V vs. Ag/AgCl (Sat.KCl) (plasma-assisted system)
N ₂ Plasma	Pt	H ₂ SO ₄	N ₂	catalyst free	0.44	32.2	2272	6	Plasma voltage 504V	[6]	6mA, catalyst-free (plasma-assisted system)
Carbon rod	TiO ₂	0.01M H ₂ SO ₄	N ₂ Plasma	catalyst free	1.52	72	4500	n.a	n.a	[7]	photo-electrocatalyst 40ml, 30min, 19mg/L
N ₂ Plasma +Pt/C	Pt/C	Deionized liquid water	N ₂ +He	0.05	0.015	n.a	560000	120	3.5V	[8]	5cm ² , 8.4w
Ru/2H-MoS ₂	Pt	0.01M HCl	N ₂	0.091	2.64*10 ⁻³	12.2	29.92 ^b	0.17	-0.15V vs. RHE	[9]	Rate of mg/h is based on 622nmol/4h pH=2 (-0.465V vs. Ag/AgCl), assume 1cm ²
Au/TiO ₂	Pt plate	0.1M HCl	N ₂	0.34	0.021	8.1	8.7 ^b	0.4	-0.2V vs. RHE	[10]	-0.456V vs. Ag/AgCl (Sat. KCl) 1cm ²
γ-Fe ₂ O ₃	IrO ₂	0.1 M KOH	N ₂	0.016	9.8*10 ⁻⁴	0.044	7.3	4.5*10 ⁻³	1.6V	[11]	Device, 338 K, assumed catalyst area of 1cm ²
Few-layer black phosphorus nanosheets	Pt	0.01M HCl	N ₂	0.51	6.3*10 ⁻³	3.1	32 ^b	1	-0.7V vs. RHE	[12]	31.37 μg h ⁻¹ mg ⁻¹ 0.2 mg catalyst Assue 1mg/cm ² pH=2 (-1V vs Ag/AgCl
THH Au NRs	Graphite plate	0.1 M KOH	N ₂	0.027	1.65*10 ⁻³	4	182 ^b	0.3	-0.2 V vs. RHE	[13]	1.648 μg h ⁻¹ cm ⁻² , 1cm ² -1V vs. Ag/AgCl
Cathode	Anode	Conditions		Ammonia Rate		FE	Specific Energy	Current	Cell	Ref.	Comments

		Electrolyte	Feed gas	nmol/cm ² s	mg/h	(%) ^a	Consumption (kWh/kgNH ₃)	Density (mA/cm ²)	potential (V)		
2D layered W ₂ N ₃ nanosheet	graphite rod	0.1 M KOH	N ₂	0.038	2.33*10 ⁻³	11.7	17.2 ^b	0.04	-0.2 V vs. RHE	[14]	1cm ² , 0.2mg/cm ² -1V vs. SCE
Pd/C	Pt mesh	0.1 M PBS	N ₂	0.022	1.35*10 ⁻³	8.2	37 ^b	0.1	0.1V vs. RHE	[15]	4.5 μg mg ⁻¹ Pd h ⁻¹ Pd/C catalyst (Pd/C loading = 1 mg cm ⁻² , with 30 wt % Pd) in 0.1 M PBS, E (vs. RHE) = E (vs. Ag/AgCl) + 0.598 V;
Fe ₂ O ₃ -CNT	Pt	Nafion/GDL	N ₂	3.6*10 ⁻³	2.2*10 ⁻⁴	0.03	35273 ^b	3.88	-2V vs. Ag/AgCl	[16]	2.2*10 ⁻³ gm ² h ⁻¹ , assumed catalyst area of 1cm ²
Au-CeO _x – RGO	Pt	0.1 M HCl	N ₂	0.136	8.3*10 ⁻³	10.1	5.5 ^b	0.1	-0.2 V vs. RHE	[17]	1cm ² , pH=1 -0.456V vs. Ag/AgCl
MOF-N-doped-C	graphite rod	0.1 M KOH	N ₂	0.944	0.014	10.2	0.017 ^b	0.2	-0.3 V vs. RHE	[18]	3.4 × 10 ⁻⁶ mol cm ⁻² h ⁻¹ 0.245 cm ² 1.2V vs Hg/HgO

^a – Faradaic efficiency (FE) at the highest rate

^b _ In the case of eNRR, energy calculated is based on the potential reported for the anode side (half-cell potential) as the total cell potential was not reported. Also, energy required to generate ultra-pure nitrogen gas also was not considered.

^c _ 64 kwh/kg NO_x for plasma side (3.5 kg is required for 1kg of ammonia), 30kWh/kg NH₃ for electrolyser and 11kwh/kg NH₃ for H-cell.

(B) Li intermediary benchmarking^d

Cathode	Anode	Conditions		Yield Rate		FE (%) ^a	Specific Energy Consumption (kWh/kg NH ₃) ^d	Current Density (mA/cm ²)	Cell potential (V)	Ref.	Comments
		Electrolyte	Feed gas	nmol/cm ² s	mg/h						
Stainless steel cloth, GDE	Pt/SSC	1 M LiBF ₄ , 0.1 M EtOH	N ₂	13.07	0.8	35	202.8-416.7 ^b	8.8	20-30V	[19]	Voltage immediately rises by the reaction time
Lithium metal on Cu	Pt Foil	1 M LiBF ₄ , 0.2 M EtOH, THF	N ₂	7.88	0.48	15.2	1.38*10 ⁶	15	23V	[20]	Energy based on 0.12W, 1.45% NH ₃ production, 5.12 nmolcm ² /s
Ag-Au@ZIF	Pt wire	0.2 M LiCF ₃ SO ₃ , ~1% EtOH, THF	N ₂	0.01	2.89*10 ⁻⁵	18	74.4	0.0158	-2.9V vs. Ag/AgCl (1M KCl)	[21]	0.047cm ² , 6h
Stainless steel cloth, flooded	Pt	[C ₄ mpyr][eFAP]	N ₂	0.023	1.4*10 ⁻³	30	11.43	0.02	-0.8 V vs. NHE	[22]	Ionic liquids 14 mg m ⁻² h ⁻¹ Assume 1cm ² , 0.8V
Molybdenum foil	Pt mesh	0.2 M LiClO ₄ , 0.18 M EtOH, THF	N ₂	0.22	0.013	7.5	1731	2.5	-9V	[23]	0.8 ± 0.1 μmol h ⁻¹ cmgeo ⁻² , 1.5h assume 1cm ²
Nickel foil	Glassy carbon	0.1 M LiCl in EDA	N ₂	0.036	0.013	17.2	50	0.06	1.8V	[24]	6cm ^{2c}
Nickel	Pt plate	LiClO ₄ , EtOH, THF	N ₂	0.26		3.8		2		[25]	2cm ²
polyimide/C	Pt	0.5 M Li ₂ SO ₄ /H ⁺	N ₂	7.7*10 ⁻³	4.7*10 ⁻⁴	2.91	164 ^c	0.1	-0.4 V vs. RHE	[26]	pH=3, -0.77V vs. Ag/AgCl

^a Faradaic efficiency (FE) at the highest rate

^b 102 μmol of ammonia was produced over the course of 130 min, with a Faradaic efficiency of 18.9%.

^c Area calculated from the rate $3.58 \times 10^{-11} \text{ mol s}^{-1} \text{ cm}^{-2}$ and amount (NH₃ for 1 h, $7.73 \times 10^{-7} \text{ mol}$).

^d Energy used to generation hydrogen gas or ethanol as one of the reactants, purification of nitrogen gas and ultra-dry electrolyte are not included for these calculations. This can significantly improve the specific energy consumption.

(C) Production of ammonia with Dielectric Barrier Discharge plasma (DBD)^a

Plasma Discharge	Plasma Parameters	Feed Gas	Flow (ml/min)	Catalyst/Electrode Material	Specific Energy Consumption (kWh/kg NH ₃)	Ref.	Comments
DBD	AC, 6kV, 10kHz	N ₂ , H ₂ (3:1)	4000	Ru/carbon nanotube	454.55	[27]	
DBD - Packed Bed	AC, 5kV, 26kHz	N ₂ , H ₂	-	Ru/Si-MCM-41	588.24	[28]	
DBD - Microgap	243.6W, 10kHz, pulse width 40 microseconds	N ₂ , CH ₄ (1:3)	500	No catalyst	1449.28	[29]	1.6s residence time, discharge gap = 0.47mm
-	DC, 0.5kV, 2mA	N ₂	-	N/A	2272.73	[6]	45-minute batch process, plasma discharge into H ₂ SO ₄ electrolyte solution
DBD	AC, 21.5 kHz, 2.5kV, 51W	N ₂ , H ₂ (1:3)	30	Tubular like Ru, Ni, Pt, Fe /Al ₂ O ₃	2631.58	[30]	2.85% conversion, decrease energy efficiency with increase power/voltage, Ru>Ni>Pt>Fe
Jet	300W, 16kHz	N ₂	30000	No catalyst	4587.22	[31]	
DBD	AC, 127W, 4.5kV, 21.5kHz	N ₂ , H ₂ (1:3)	30	Ru on membrane like alumina	12500.00	[32]	
Jet Glow	AC, 8.4W, 20kHz	N ₂ , He (1:1), H ₂ O	2500	Pt/C	560000	[8]	Only 20% plasma exposure on catalyst surface

^a high temperature or vacuum-based systems are not included in this table

(d) Production of NO_x with plasma^a

Plasma Discharge	Plasma Parameters	Pressure (kPa)	Temperature (K)	Feed Gas	Flow (mL/min)	Total NO _x (mg/min)	Specific Energy Consumption (kWh/kg NO _x)	Ref.	Comments
DRGSD with Raschig rings	AC, 8.4kV, 11.27W	ambient	ambient	Air	2000	2.92	64	This work	
Spark	AC, 25kHz, 3.5kV	ambient	ambient	ambient air	N/A	0.38	N/A	[33]	
Multi-spark discharge system	100W, 10kV	ambient	ambient	ambient air	N/A	6.00	278	[34]	181 mg/L (85mg/L (NO ₂ ⁻) + 96mg/L(NO ₃ ⁻)),4L, 120min
Plasma Jet	30kHz, 10kV (pp), 0.47W	ambient	ambient	Air, He	500 (He), Ambient Air	0.00037	17000	[35]	1.35 mg/L (0.7mg/L(NO ₂ ⁻) + 0.65mg/L (NO ₃ ⁻)), 4.1mL. 15min
WS (Water Sealed)-DBD	10kHz, 8.14W	ambient	ambient	Air	500	0.74	183	[36]	
Wire-in-nozzle (glow)	10kHz, 7.6W	ambient	ambient	Air	1000	0.30	428		
Wire-in-nozzle (spark)	10kHz, 51.3W	ambient	ambient	Air	1000	1.62	530		
Pin-to-water	0.16kHz, 10W	ambient	ambient	Air	1000	0.30	560		
Plasma Jet	DC, 5kHz,7kV, 1.5W	ambient	ambient	N ₂ (80%), O ₂ (20%), He	10 (N ₂ ,O ₂), 5000 (He)	0.02	1230	[37]	

^a high temperature or vacuum-based systems are not included in this table

Movie S1. Single reactor glow discharge (SRGD)

Movie S2. Single reactor spark discharge (SRSD)

Movie S3. Single reactor glow and spark discharge (SRGSD)

Movie S4. Double reactor glow and spark discharge (DRGSD)

Movie S5. Double reactor glow and spark discharge with Raschig Rings

Movie S6. Plasma discharges inside forming bubbles

References

1. Wang, Y., et al., *Unveiling the Activity Origin of a Copper - based Electrocatalyst for Selective Nitrate Reduction to Ammonia*. *Angewandte Chemie*, 2020. **132**(13): p. 5388-5392.
2. Bard, A., *Standard potentials in aqueous solution*. 2017: Routledge.
3. Pérez-Gallent, E., et al., *Electrocatalytic reduction of Nitrate on Copper single crystals in acidic and alkaline solutions*. *Electrochimica Acta*, 2017. **227**: p. 77-84.
4. Jingjing, L. and H. Xiao, *Contrasting behaviours of AC and DC excited plasmas in contact with liquid*. *Plasma Science and Technology*, 2013. **15**(8): p. 768.
5. Zhou, R., et al., *Microplasma bubbles: reactive vehicles for biofilm dispersal*. *ACS applied materials & interfaces*, 2019. **11**(23): p. 20660-20669.
6. Hawtof, R., et al., *Catalyst-free, highly selective synthesis of ammonia from nitrogen and water by a plasma electrolytic system*. *Sci Adv*, 2019. **5**(1): p. eaat5778.
7. Lamichhane, P., et al., *Sustainable nitrogen fixation from synergistic effect of photo-electrochemical water splitting and atmospheric pressure N₂ plasma*. *Plasma Sources Science and Technology*, 2020. **29**(4): p. 045026.
8. Kumari, S., et al., *Synergistic plasma-assisted electrochemical reduction of nitrogen to ammonia*. *Chemical communications*, 2018. **54**(95): p. 13347-13350.
9. Surrnto, B.H.R., et al., *MoS₂ Polymorphic Engineering Enhances Selectivity in the Electrochemical Reduction of Nitrogen to Ammonia*. *Acs Energy Letters*, 2019. **4**(2): p. 430-435.
10. Shi, M.M., et al., *Au sub - nanoclusters on TiO₂ toward highly efficient and selective electrocatalyst for N₂ conversion to NH₃ at ambient conditions*. *Advanced Materials*, 2017. **29**(17): p. 1606550.
11. Kong, J., et al., *Electrochemical synthesis of NH₃ at low temperature and atmospheric pressure using a γ -Fe₂O₃ catalyst*. *ACS Sustainable Chemistry & Engineering*, 2017. **5**(11): p. 10986-10995.
12. Zhang, L., et al., *Ammonia synthesis under ambient conditions: Selective electroreduction of dinitrogen to ammonia on black phosphorus nanosheets*. *Angewandte Chemie*, 2019. **131**(9): p. 2638-2642.
13. Bao, D., et al., *Electrochemical reduction of N₂ under ambient conditions for artificial N₂ fixation and renewable energy storage using N₂/NH₃ cycle*. *Advanced materials*, 2017. **29**(3): p. 1604799.
14. Jin, H.Y., et al., *Nitrogen Vacancies on 2D Layered W₂N₃: A Stable and Efficient Active Site for Nitrogen Reduction Reaction*. *Advanced Materials*, 2019. **31**(32).
15. Wang, J., et al., *Ambient ammonia synthesis via palladium-catalyzed electrohydrogenation of dinitrogen at low overpotential*. *Nature communications*, 2018. **9**(1): p. 1-7.
16. Chen, S., et al., *Electrocatalytic Synthesis of Ammonia at Room Temperature and Atmospheric Pressure from Water and Nitrogen on a Carbon - Nanotube - Based Electrocatalyst*. *Angewandte Chemie International Edition*, 2017. **56**(10): p. 2699-2703.
17. Li, S.J., et al., *Amorphizing of Au nanoparticles by CeO_x-RGO hybrid support towards highly efficient electrocatalyst for N₂ reduction under ambient conditions*. *Advanced materials*, 2017. **29**(33): p. 1700001.
18. Mukherjee, S., et al., *Metal-organic framework-derived nitrogen-doped highly disordered carbon for electrochemical ammonia synthesis using N₂ and H₂O in alkaline electrolytes*. *Nano Energy*, 2018. **48**: p. 217-226.

19. Lazouski, N., et al., *Non-aqueous gas diffusion electrodes for rapid ammonia synthesis from nitrogen and water-splitting-derived hydrogen*. *Nature Catalysis*, 2020. **3**(5): p. 463-+.
20. Lazouski, N., et al., *Understanding Continuous Lithium-Mediated Electrochemical Nitrogen Reduction*. *Joule*, 2019. **3**(4): p. 1127-1139.
21. Lee, H.K., et al., *Favoring the unfavored: Selective electrochemical nitrogen fixation using a reticular chemistry approach*. *Science Advances*, 2018. **4**(3).
22. Zhou, F.L., et al., *Electro-synthesis of ammonia from nitrogen at ambient temperature and pressure in ionic liquids*. *Energy & Environmental Science*, 2017. **10**(12): p. 2516-2520.
23. Andersen, S.Z., et al., *A rigorous electrochemical ammonia synthesis protocol with quantitative isotope measurements*. *Nature*, 2019. **570**(7762): p. 504-508.
24. Kim, K., et al., *Electrochemical synthesis of ammonia from water and nitrogen in ethylenediamine under ambient temperature and pressure*. *Journal of The Electrochemical Society*, 2016. **163**(14): p. F1523-F1526.
25. Pappenfus, T.M., et al., *Wind to ammonia: Electrochemical processes in room temperature ionic liquids*. *ECS Transactions*, 2009. **16**(49): p. 89.
26. Chen, G.-F., et al., *Ammonia electrosynthesis with high selectivity under ambient conditions via a Li⁺ incorporation strategy*. *Journal of the American Chemical Society*, 2017. **139**(29): p. 9771-9774.
27. Peng, P., et al., *Atmospheric pressure ammonia synthesis using non-thermal plasma assisted catalysis*. *Plasma Chemistry and Plasma Processing*, 2016. **36**(5): p. 1201-1210.
28. Peng, P., et al., *Ru-based multifunctional mesoporous catalyst for low-pressure and non-thermal plasma synthesis of ammonia*. *International Journal of Hydrogen Energy*, 2017. **42**(30): p. 19056-19066.
29. Bai, M., et al., *Synthesis of ammonia using CH₄/N₂ plasmas based on micro-gap discharge under environmentally friendly condition*. *Plasma Chemistry and Plasma Processing*, 2008. **28**(4): p. 405-414.
30. Mizushima, T., et al., *Tubular membrane-like catalyst for reactor with dielectric-barrier-discharge plasma and its performance in ammonia synthesis*. *Applied catalysis a: general*, 2004. **265**(1): p. 53-59.
31. Kubota, Y., et al., *Synthesis of ammonia through direct chemical reactions between an atmospheric nitrogen plasma jet and a liquid*. *Plasma and Fusion Research*, 2010. **5**: p. 042-042.
32. Mizushima, T., et al., *Catalytic effects of metal-loaded membrane-like alumina tubes on ammonia synthesis in atmospheric pressure plasma by dielectric barrier discharge*. *Plasma Chemistry and Plasma Processing*, 2007. **27**(1): p. 1-11.
33. Lu, P., et al., *Achieving reactive species specificity within plasma - activated water through selective generation using air spark and glow discharges*. *Plasma Processes and Polymers*, 2017. **14**(8): p. 1600207.
34. Nakaso, T., et al. *Multi-spark discharge system for preparation of nutritious water*. in *AIP Conference Proceedings*. 2018. AIP Publishing LLC.
35. Ogawa, K., et al., *Modulating the concentrations of reactive oxygen and nitrogen species and oxygen in water with helium and argon gas and plasma jets*. *Japanese Journal of Applied Physics*, 2018. **58**(SA): p. SAAB01.
36. Tachibana, K. and T. Nakamura, *Comparative study of discharge schemes for production rates and ratios of reactive oxygen and nitrogen species in plasma activated water*. *Journal of Physics D: Applied Physics*, 2019. **52**(38): p. 385202.

37. Uchida, G., et al., *Selective production of reactive oxygen and nitrogen species in the plasma-treated water by using a nonthermal high-frequency plasma jet*. Japanese Journal of Applied Physics, 2017. **57**(1): p. 0102B4.